On modelling the constitutive and damage behaviour of highly non-linear bio-composites – mesh sensitivity of the viscoplastic-damage law computations

C. G. Skamniotis[a], M. Elliott[b], M. N. Charalambides[a]

[a] Department of Mechanical Engineering, Imperial College London, London SW7 2AZ, United Kingdom
[b] Mars Petcare, Oakwell Way, Birstall, Batley, WF17 9LU, United Kingdom
E-mail: c.skamniotis13@imperial.ac.uk; m.charalambides@imperial.ac.uk

ABSTRACT

The large strain fracture of non-linear complex solids concerns a wide range of applications, such as material forming, food oral processing, surgical instrumental penetration as well as more recently, the design of biodegradable composites for packaging and bio-medical use. Although computer simulations is a powerful technology towards understanding and designing such processes, modelling ductile fracture in soft natural composites imposes a new challenge, particularly when the fracture patterns cannot be pre-defined. Here we bring to light new information on these aspects of benefit to the multidisciplinary community, by characterising and modelling the deformation and fracture of short cellulose fibre starch extruded composites. Hyperviscoelastic-Mullins damage laws show merits in modelling such complex systems. Yet they are inferior to a viscoplastic-damage law able to capture exactly their highly non-linear, rate dependent and pressure dependent pseudo-plastic stress-strain response. It also predicts fracture based on experimental toughness values without pre-specifying the crack path in a Finite Element (FE) model, displaying superiority over the conventional cohesive zone approach. Yet, despite using a toughness parameter to drive crack propagation, spurious mesh dependency is still observed while other previously unreported sources of error imposed by the finite element aspect ratio are also highlighted. The latter is rectified by developing a novel numerical strategy for calculating the characteristic element length used in the damage computations. Inherent mesh dependency is however not resolved, suggesting that non-local damage models may be essential to model this newly investigated class of natural composites.

Keywords: A. Fracture toughness, B. Viscoplastic-damage model, C. Mesh dependency, Starch-fibre composite, Characteristic element length

1 Introduction

An emerging field in material science and engineering is the design of renewable biodegradable plastics/composites for packaging (Majeed, Jawaid et al. 2013) as well as bio-medical use (Cai, Zhang et al. , Fernandes, Pires et al. 2013). This owes to requirements for low manufacturing costs, shortage of petroleum sources, and to the unique physicochemical and thermo-mechanical characteristics of polymers (Zakaria, Muhammad et al. 2017). Furthermore, developing bio-degradable plastics/composites is of critical importance to the community, as synthetic materials do not degrade into soil causing environmental problems with direct impact on human health (Ali, Unnikrishnan et al. 2013). In this regard, environmentally friendly materials such as starch now receive considerable attention (Hbib, Guessasma et al. 2011, Majeed, Jawaid et al. 2013, Zakaria, Muhammad et al. 2017). Starch is a versatile polymer, abundant in nature, which can be processed and/or reinforced to modify its mechanical strength and hydration properties in order to serve as a packaging (Taguet, Bureau et al. 2014), self-healing (Voyiadjis, Shojaei et al. 2011) and shape memory material (Meng and Li 2013), not least as a main ingredient in commercial food products (Skamniotis, Patel et al. 2016). Moreover, starch displays a high biocompatibility and solubility profile which makes it useful for various biomedical-pharmaceutical applications (Zhao, Yao et al. 2015) such as bone replacement and carriage of drugs for controlled delivery of bioactive agents (Zakaria, Muhammad et al. 2017). These are technologically demanding applications which cannot afford to rely on empirical knowledge/design. This has increased the need for computational modelling tools to aid in both understanding and optimising such processes, particularly when biological systems are difficult to access *in-vivo* (Jin 2014).

However, although modern commercial FE software (Simulia 2013) and other advanced multiscale modelling techniques (Digimat 2011) offer extensive material modelling capabilities, capturing the large strain response of complex, soft bio-composites such as cellulose fibre reinforced starch extrudates consists a new challenge (Chivrac, Gueguen et al. 2008, Guessasma, Sehaki et al. 2008, Madsen, Joffe et al. 2011), especially when complex damage/fracture patterns are involved. This is attributed to:

- limited previous work on mechanical characterisation and material modelling of such systems,
- limited applicability of available analytical/numerical micromechanical models for fibre reinforcement mechanisms as well as anisotropic constitutive models, due to a large uncertainty in the degree of fibre orientation and fibre-matrix interaction properties after the extrusion-cooking process takes place (Skamniotis, Patel et al. 2018),
- inherent complex behaviour of extruded starch-fibre systems, associated with high non-linearity, large energy dissipation and fracture toughness, as well as strong time dependency and stress state dependency (Guessasma, Sehaki et al. 2008, Bergstrom 2015, Skamniotis, Kamaludin et al. 2017),
- and finally longstanding difficulties in modelling large strain fracture based on experimental fracture toughness values without predefining the crack path (Hedjazi, Guessasma et al. 2011, Mohammed P. Afandi, Charalambides et al. 2013, Oldfield, Dini et al. 2013).

Our work aims to provide a fundamental step forward towards addressing the above challenges, by using an isotropic continuum damage mechanics coupled with a fracture mechanics approach. Although from a material modelling point of view a simplistic approach is employed, yet this is a necessary step for the newly investigated materials considered here, before introducing additional complexity i.e. anisotropic plasticity and anisotropic damage. Consequently, emphasis is here

given on the applicability of various available constitutive law theories and numerical strategies to starch-fibre extruded soft composites.

To start with, the hyperviscoelastic laws combined with Mullins effect have shown merits in predicting challenging constitutive stress-strain behaviours (Hagan 2009, Ayoub, Zaïri et al. 2014, Su, Yang et al. 2016, Wheatley, Morrow et al. 2016, Mohammed P. Afandi, Wanigasooriya et al. 2017, Wang and Chester 2017). They have been also successfully coupled with cohesive traction-separation laws originated from fracture mechanics principles, to model material separation along a cohesive layer based on experimental fracture toughness, G_c (kJ/m²), values (Gao and Bower 2004, Mohammed P. Afandi, Charalambides et al. 2013, Oldfield, Dini et al. 2013, Arora, Tarleton et al. 2015). However, this has been possible upon insertion of special purpose cohesive elements in an FE mesh, assuming a prior knowledge of the fracture path, which is not true in various applications i.e. when multi-axial loading and complex geometries are involved (Skamniotis, Patel et al. 2016). More recently, the adaptive or automatic insertion of multiple cohesive elements in a mesh has been shown to provide solutions in predicting arbitrary fracture paths (Paulino, Celes et al. 2008, Oldfield, Dini et al. 2010, He and Li 2012, Oldfield, Dini et al. 2013, Ponnusami, Turteltaub et al. 2015, Shor and Vaziri 2015, Wang, Zhang et al. 2016). However, the approach requires considerable effort to implement while its applicability and computational cost are limiting factors for large FE models, particularly when these involve large deformations (Harrison, Cleary et al. 2014, Skamniotis, Elliott et al. 2017).

On the other hand, these limitations do not seem to be a concern when separation is modelled by allowing any element in an FE mesh to undergo damage and subsequent element deletion based on continuum damage mechanics concepts (Abendroth and Kuna 2006, Badreddine, Saanouni et al. 2010, Belnoue, Garnham et al. 2010, Xue, Pontin et al. 2010, Smojver and Ivančević 2011, Hambli 2013, Mohammed, Charalambides et al. 2014, Skamniotis, Patel et al. 2016). This enables predicting challenging deformation and damage phenomena, including complex material separation patterns (Badreddine, Saanouni et al. 2010, Lee, Steglich et al. 2017, Skamniotis, Elliott et al. 2017) and surface erosion (Lv, Huang et al. 2015). The advantage of this approach over the cohesive zone technique is that constitutive laws governing the undamaged material behaviour are coupled with damage laws in the same FE material model definition (Simulia 2013).

A great deal of work has been devoted to developing such models in order to combine the constitutive elasto-plastic material behaviour with the progressive stiffness degradation and subsequent fracture due to the nucleation, growth and coalescence of voids/microcracks as well as other damage processes (Zaïri, Naït-Abdelaziz et al. 2008, Haddag, Abed-Meraim et al. 2009, Bai and Wierzbicki 2010, Luo and Wierzbicki 2010, Xue, Pontin et al. 2010, Vignjevic, Djordjevic et al. 2012, Pack, Luo et al. 2014, Rousselier and Luo 2014, Safaei, Lee et al. 2015, Lawrimore II, Francis et al. 2016, Cheng and Ghosh 2017). Basaran and Yan (Basaran and Yan 1998) were the first to correlate these damage processes with entropy production rate in order to introduce damage evolution functions derived from statistical thermodynamic principles. Since then, thermodynamic models have been developed further to describe damage in a range of solids based on physical parameters (Voyiadjis, Shojaei et al. 2011, Yao and Basaran 2013, Alfano and Musto 2017), whereas other empirical/phenomenological damage models have also found extensive use (Shutov, Silbermann et al. 2015). Voyiadjis *et al.* (Voyiadjis, Shojaei et al. 2011) constructed a mathematical framework which incorporates the elastic, plastic, damage as well as recovery/healing components of the uniaxial compression response in shape memory polymers. Alinaghian *et al.* (Alinaghian, Asadi et al. 2014) presented an FE model predicting the effect of pre-strain on void growth and ultimate fracture. On the other hand, Rousselier *et al. (Rousselier*

and Luo 2014) report on fracture FE simulations between varying stress states applied in aluminium specimens based on a void damage coupled with the Mohr-Coulomb material model, while Pack *et al.* (Pack, Luo et al. 2014) used a similar material model to predict complex crack initiation and propagation patterns in modified compact tension specimens and highlighted the effect of mesh refinement on the results. Recently, Lee *et al.* (Lee, Steglich et al. 2017) took into account both the stress state dependence of fracture strain as well as material anisotropy in order to simulate the ductile fracture of magnesium alloys without previous knowledge of the crack patterns.

However, the former studies reported numerical results highly sensitive to the mesh density when the classical continuum local damage approach is applied (Abu Al-Rub and Voyiadjis 2009). This is because the absence of a physical material length scale, ℓ, as a localization limiter implies that when damage and/or yielding initiates, the width of the localised deformation is subject to the size (or length) of the finite elements, L_{ch}, used in the mesh (Voyiadjis and Dorgan 2004). This issue has been under intensive research over the last three decades and has been tackled through various numerical strategies (Abu Al-Rub and Voyiadjis 2009, Badreddine, Saanouni et al. 2010, Verhoosel, Scott et al. 2011, Vignjevic, Djordjevic et al. 2012, Rousselier and Luo 2014, Vignjevic, Djordjevic et al. 2014), amongst them the most popular are the nonlocal integral weighted average approach (Ferrara and Prisco 2001) and the gradient-enhanced approach (Abu Al-Rub and Voyiadjis 2009) originally proposed by De Borst et al. (De Borst and Mühlhaus 1992). The latter involves calculating a nonlocal damage variable upon which the damage state at a material point/element is influenced by the state of its neighbouring elements. This ensures that damage is encountered in a number of elements within a zone of which the dimensions are determined by ℓ and not by L_{ch}. For example, in crystalline systems ℓ has been related to grain size while in composites it is associated with the size of inclusions (Al-Rub and Kamel 2004). However, experimental G_c values have been rarely used and/or related to ℓ in the literature, in order to model crack propagation through the non local damage technique based on a G_c criterion. This could be due to G_c not being a critical parameter for damage in metal processes, potentially due to a less significant energy required to create new surface areas compared to the energy involved in plastic flow. On the other hand, the opposite is the case in biological materials, natural composites and generally soft solids (Ji and Gao 2004, Tanaka 2007, Launey and Ritchie 2009, Barthelat and Rabiei 2011, Bhattacharjee, Barlingay et al. 2013, Zhang, Lin et al. 2015, Lavagna, Massella et al. 2018), especially in the starch-fibre systems studied here where G_c has been recently highlighted as a major determinant of fracture (Skamniotis, Kamaludin et al. 2017). Consequently, the implementation of a strict G_c criterion, determined by experiments, is of particular importance in this investigation. In other words, emphasis is given on modelling fracture through a unified damage mechanics-fracture mechanics approach.

In order to address the above, it is useful to recognise that the inherent unacceptable mesh dependency imposed by conventional local damage models has been mainly associated with the use of strain softening laws (Abu Al-Rub and Voyiadjis 2009, Le, Marigo et al. 2018). Instead, much less work has focused on using a G_c driven softening law, such that softening evolves as a function of element elongation (Arefi, van der Meer et al. 2018, van Dongen, van Oostrum et al. 2018), also widely referred as effective element displacement. The latter approach was originally introduced by Hilleborg et al. (Hillerborg, Modéer et al. 1976) in order to unify the fracture mechanics and damage mechanics theories (van Dongen, van Oostrum et al. 2018). The law postulates damage evolution based on a consistent energy dissipation per surface area regardless

of the finite element size i.e. similar to the cohesive zone approach, and is thus incorporated in commercial FE software (Simulia 2013) as a mesh independent measure for modelling crack propagation without specifying the crack path (Arefi, van der Meer et al. 2018). However, to which extent mesh dependency is in fact rectified has not been rigorously investigated, while the accuracy of this approach in predicting crack propagation for known G_c values is not well established i.e. through validating by fracture experiments. Furthermore, mesh sensitivity related to other factors which do come into play in this approach i.e. element aspect ratio, is unexplored.

All these longstanding questions are tackled here, while the merits of damage models defined by a G_c driven softening law in modelling the large strain fracture of soft bio-composites are also investigated. Bridging these knowledge gaps first, particularly in these newly investigated complex materials, was considered necessary prior to using alternative and more advanced non local damage approaches, as well as entropy based damage models. This is performed through mechanical characterisation and modelling of the stress-strain and fracture response of soft starch extrudates reinforced by short cellulose fibres; this composition is also being used in pet food applications (Skamniotis, Kamaludin et al. 2017). A description of the material and experimental-numerical methods is firstly provided followed by a presentation of the relevant theory. Thereafter, new material model calibration techniques are developed for the hyperviscoelastic coupled with Mullins damage and viscoplastic coupled with ductile damage models. These are fitted to the compression and tensile test data of the starch composite and the experimental-model match is discussed and compared. Thereafter, the merits of the viscoplastic with ductile damage law in predicting crack initiation and propagation based on a previously determined G_c value (Skamniotis, Kamaludin et al. 2017) are studied by modelling an independent tensile fracture experiment. An extensive mesh sensitivity analysis is finally performed.

Our study identifies current implications related to modelling the complex behaviour of soft extruded starch bio-composites and presents new material constitutive law options. These laws are able to capture a wide range of different non-linear, time-dependent and stress-state dependent stress-strain responses including damage up to ultimate fracture. These are critical tools for the design of applications involving large strain fracture under multi-axial loading, particularly when the material G_c parameter is critical.

2 Materials and methods

2.1 Material

The material was extruded in the form of rectangular and square cross section profiles by Mars Petcare UK, with w/w composition: 47.5% starch (15−20 μm raw granule size), 2.5% cellulose fibres (200−500 μm length and 20−30 μm diameter) and 50% water. Previous experiments (Skamniotis, Patel et al. 2016) suggested insignificant anisotropy in the stress-strain response, yet with a potential directional dependency in G_c. The former was due to the absence of the fibre bridging mechanism at the crack tip during fracture when the material was stretched perpendicularly to the principal extrusion axis. However, for the purposes of this study, fracture is here only induced by stretching the material along the extrusion direction for which G_c values are also available (Skamniotis, Kamaludin et al. 2017). The potential degree of fibre alignment to the extrusion axis was therefore not investigated. Moisture loss effects were prevented by keeping the samples sealed after production until testing. Ageing effects through starch re-crystallization (Moscicki, Mitrus et al. 2013) were eliminated by conducting all the tests consistently three weeks after production and within three consecutive days. A constant temperature of 20 $°C$ and relative humidity of 50 % were maintained for all the experiments.

2.2 Experimental

2.2.1 Uniaxial tension & compression

The experimental procedure involves monotonic, stress relaxation as well as loading-unloading tests in both compression and tension using the cuboid (height x square edge = 13 x 8 mm) specimens shown in Figure 1(b) and the dumbbell (grip to grip length x width x thickness = 100 x 12 x 5 mm) specimens displayed in Figure 1(a), respectively. The cuboid and dumbbell specimens were manually cut from the square and rectangular extrudate profiles, correspondingly, using specimen dies and a mechanical press (Skamniotis, Kamaludin et al. 2017). True tensile strain was calculated based on subsequent optical measurements of an original gauge length of $L_o = 40$ mm which was marked on the dumbbells prior to the test. All the experiments reported in this manuscript were conducted via a single column Zwick Roell universal testing machine (1kN load cell capacity) with true strain rate control based on the predefined grip to grip original length of 100 mm; serrated tensile grips ensured no grip-specimen slippage. Preliminary tests indicated that the true strain determined based on gauge length measurements is consistently only 3% larger than the true strain calculated based on the grip machine displacement data, while this difference was practically constant throughout each test. Therefore, it was reasonable to assume that the strain rates which were in fact applied in the gauge length were equal to the strain rates prescribed on the machine (selected strain rate values given in next paragraph). The compressive specimen dimensions are chosen based on results of a preliminary study of friction effects/barrelling on the stress-strain, $\sigma - \varepsilon$, calculations; these indicated that a height over square edge ratio of $L_o/D_o \geq 13/8$ reduces sample-platen friction effects on the $\sigma - \varepsilon$ results for strains up to 0.8, as suggested by Charalambides *et al.* (Charalambides, Goh et al. 2005). These effects are further minimised by attaching polyetrafluoroethylene (PTFE) sheets (0.5 mm thickness) on the platens and lubricating with silicon oil of 0.1 m²/s viscosity (see Figure 1(b)).

Time dependency was studied through monotonic tests at the four constant true strain rates, $\dot{\varepsilon} =$ 0.0001/s, 0.01/s, 0.1/s, 1/s, each repeated five times; each rate also provided a tensile failure strain, $\varepsilon_f(\dot{\varepsilon})$. Relaxation data were collected for absolute strains, ε = 0.1, 0.2, 0.5 in compression and ε = 0.03, 0.06, 0.08 in tension; these were held constant for twenty minutes while an initial $\dot{\varepsilon} =$ 0.01/s ramp loading was applied. Two test repeats were used. Loading-unloading was performed at $\varepsilon =$ 0.2, 0.5, 0.8 in compression and $\varepsilon =$ 0.07, 0.2, 0.22 in tension, both performed at two rates, $\dot{\varepsilon} =$ 0.1, 1/s and using two test repeats. For force, F, and current specimen cross sectional area, A_i, the true (Cauchy) stress is obtained by:

$$\sigma = \frac{F}{A_i} \tag{1}$$

while the true (Hencky) strain is given by:

$$\varepsilon = \ln\left(\frac{L_i}{L_o}\right) \tag{2}$$

where L_o and L_i are the original and current specimen length, respectively; note that length refers to specimen height in compression and gauge length in tension. Incompressibility was assumed based on a Poisson's ratio, $\nu = 0.5$ already found for this material (Skamniotis, Patel et al. 2016). The calculation of true strain based on grip machine displacement, δ, was performed through Equation (2) by using L_o = 100 mm and $L_i = L_o + \delta$.

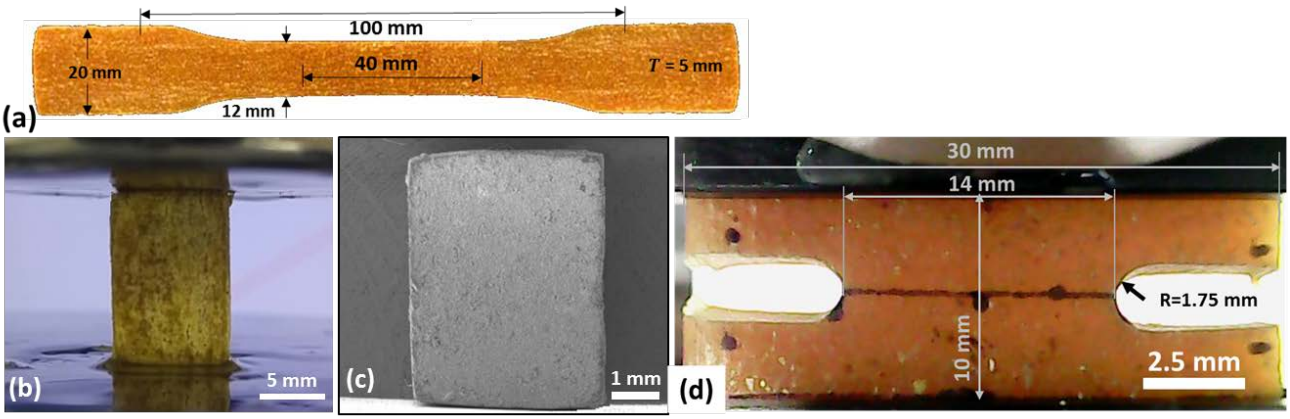

Figure 1. Experimental configurations: (a) uniaxial tensile dumbbell specimen, (b) uniaxial compression test, (c) in-situ SEM uniaxial compression test, (d) fracture experiment.

2.2.2 Microscopy analysis

Scanning Electron Microscopy (SEM) data, obtained via a Hitachi S-3400N equipment, also reveal how the microstructure evolves with deformation. This includes the *in-situ* SEM compression test (10kV, 56.8 mm, x60) displayed by Figure 1(c) on small cuboid specimens (height x square edge = 6 x 4 mm) with the aid of a micro-tester (200 N load cell capacity) and the post fracture SEM observations of specimens used in uniaxial tension (shown later in Figure 10).

2.2.3 Fracture experiment

An additional fracture experiment, depicted in Figure 1(d), investigates the crack initiation and propagation behaviour. It resembles the double-edge-notched-tension (DENT) geometry but with blunt notches of $R = 1.75$ mm radius. Specimens of 10x30x5 mm (length x width x thickness) are used (see Figure 1(d)) with a ligament length of 14 mm between the two notches; these are created via pushing a cylindrical cutting die across the specimen thickness. A displacement rate of $\dot{\delta} =$ 1000 mm/min is applied while the test is repeated five times and the average force-displacement, $F - \delta$, curve is computed.

2.3 Numerical

The uniaxial tension and compression data are utilised to investigate the suitability of two relevant material models available in the literature. In addition, the $F - \delta$ data of the fracture experiment are compared against the corresponding predictions of a viscoplastic-damage material model. This involves simulating the experimental deformation and fracture events based on a fracture toughness of $G_c = 0.93$ kJ/m² previously determined for this material (Skamniotis, Kamaludin et al. 2017); the latter was found to be independent of rate.

The corresponding FE model involves the 3D mesh shown in Figure 2(a) simulating a quarter of the fracture specimen due to symmetry; this requires symmetry boundary conditions as denoted in Figure 2(a) and 2(b). A 3D model is used as it was not known whether plane strain or plane stress conditions prevail. The bottom surface is fixed while the top surface is constrained in all translations and rotations apart from the Y-axis along which the $\dot{\delta} = 1000$ mm/min condition is applied. The dynamic explicit analysis of the commercial FE software ABAQUS 2016 (Simulia 2013) is used, based on the true material density 1410 kg/m^2 and semi-automatic mass scaling with maximum target increment $\Delta t_t = 10^{-5}$ s, while ensuring that the total kinetic energy is less than 2% of the total internal energy such that inertia effects are insignificant (Skamniotis, Patel et al. 2016). A Poisson's ratio of $\nu = 0.49$ is used instead of the true $\nu = 0.5$, due to numerical restrictions induced by the Explicit analysis (Simulia 2013).

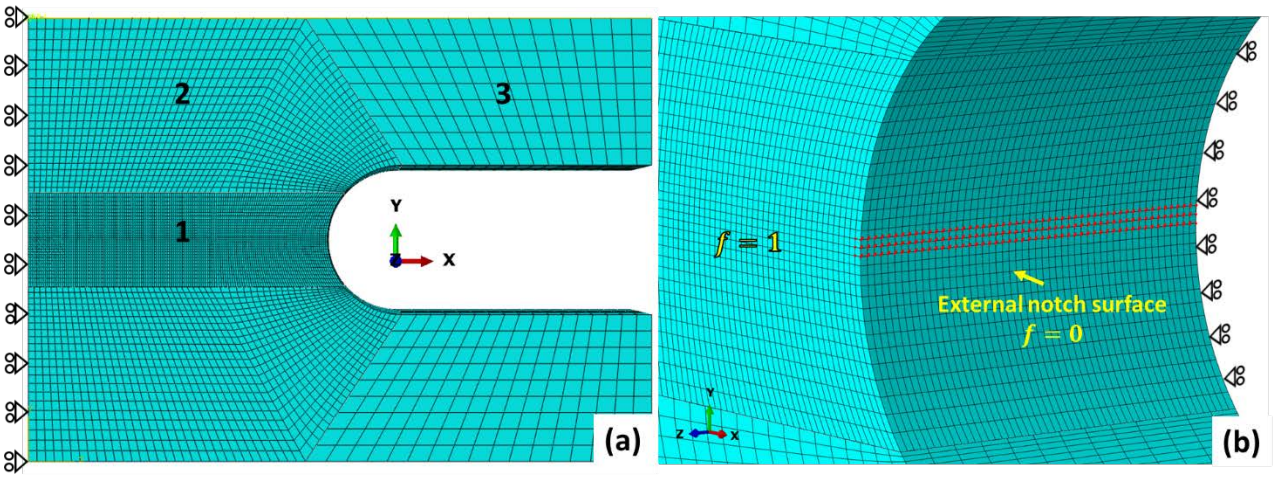

Figure 2. FE model of the verification test: (a) side view of the model mesh, (b) notch tip detail; the elements of the notch tip are highlighted in red and the different predefined field variables, f, are denoted.

The mesh consists of 235420 3D stress-displacement reduced integration hexahedral linear eight node elements and two tie constraints: one between the coarse mesh region '3' (see Figure 2(a)) (very low strains) and the less coarse region '2', as well as one between region '2' and the fine mesh region '1' (large strains). A mesh sensitivity analysis is performed by varying the element sizes uniformly in region '1' based on a characteristic element length parameter, L_{ch}, in the range 0.02 – 0.2 mm. The theoretical concept of L_{ch} is also investigated by comparing the viscoplastic-damage law single element simulation predictions based on two different L_{ch} calculation methods. The following section describes the calibration of suitable material models.

3 Material modelling

3.1 Hyperviscoelastic-Mullins model

The Hyperviscoelastic-Mullins material model used here combines a second order Ogden hyperelastic law, Prony series and the Mullins damage effect, which respectively account for strain dependency, time dependency and strain history dependency in the computed global stress (Ayoub, Zaïri et al. 2014, Mohammed P. Afandi, Wanigasooriya et al. 2017). This can be concisely expressed by the following modified recursive formula developed based on the Generalized Maxwell Model (Goh, Charalambides et al. 2004):

$$\sigma\left(\varepsilon_{t_{n+1}}, t_{n+1}\right) = \tilde{\eta} g_{\infty} \sigma_o\left(\varepsilon_{t_{n+1}}\right) + \sum_{i=1}^{n} \left(\sigma_i\left(\varepsilon_{t_n}, t_n\right) e^{-\frac{\Delta t}{\tau_i}} + g_i \frac{\left(1 - e^{-\frac{\Delta t}{\tau_i}}\right)}{\frac{\Delta t}{\tau_i}} \left(\sigma_o\left(\varepsilon_{t_{n+1}}\right) - \sigma_o\left(\varepsilon_{t_n}\right)\right) \right) \quad (3)$$

where $\sigma\left(\varepsilon_{t_{n+1}}, t_{n+1}\right)$ is the global stress at time t_{n+1}, n is the total number of Maxwell elements, τ_i is the relaxation time for each i element, g_i is the weighted contribution of each i element to the global stress, g_∞ is the contribution of the equilibrium (long-term) element to the global stress ($g_\infty + \sum_{i=1}^{n} g_i = 1$), $\Delta t = t_{n+1} - t_n$ are finite time increments associated with strain dependent (instantaneous) stresses $\sigma_o\left(\varepsilon_{t_{n+1}}\right)$ and $\sigma_o\left(\varepsilon_{t_n}\right)$, $\sigma_i\left(\varepsilon_{t_n}, t_n\right)$ is the i element stress and $\tilde{\eta}$ is the Mullins damage variable. A detailed description of the above terms and the underlining theory of hyperviscoelasticity and Mullins damage effect can be found elsewhere (Hurtado, Lapczyk et al. 2013, Simulia 2013, Ayoub, Zaïri et al. 2014, Bergstrom 2015).

The strain dependent (instantaneous), $\sigma_o(\varepsilon)$, terms are computed assuming incompressibility based on the Ogden hyperelastic strain energy density function for uniaxial deformation in terms of the stretch ratio, $\lambda = e^{\varepsilon}$, via:

$$\sigma_o(\lambda) = \sum_{i=1}^{N} \frac{2\mu_i}{a_i}\left(\lambda^{a_i} - \lambda^{-\frac{a_i}{2}}\right) \tag{4}$$

where N is the order of the potential ($N = 2$ here), a_i, D_i are material parameters and the terms μ_i define the initial shear modulus, $\mu = \sum_{i=1}^{N} \mu_i$. Amongst a variety of other functions available, including the Mooney-Rivlin, Polynomial, Van der Waals, Arruda-Boyce, Marlow, Neo-Hookean, Yeoh (Simulia 2013, Bergstrom 2015), the Ogden function was found to give the best experimental-model fit for both compression and tension here.

The Ogden, Prony and Mullins material constants are determined by implementing Equation (3) in an MS Excel numerical solver (Generalized Reduced Gradient Nonlinear Engine) where the model predictions are matched with the test data via minimizing an experimental-model error variable (Hagan, Charalambides et al. 2011, Simulia 2013); a detailed description the method can be found in (Hagan 2009). Here, calibration involved five Prony terms ($n = 5$) from which the g_i terms were varied while the τ_i terms initially remained constant at 0.01, 0.1, 1, 10, 1000 s. At the end of the iterations, the τ_i terms were re-calibrated empirically to improve further the fit (Hagan 2009, Mohammed P. Afandi, Charalambides et al. 2013).

Thereafter, the calibration of the Mullins parameters was performed independently based on the loading-unloading data. Specifically, $\tilde{\eta}$ introduces stress softening by scaling down the equilibrium (long term) response (see Equation (3)) by varying monotonically between $0 < \tilde{\eta} \leq 1$ depending on the current stored energy density U and its maximum value, U_{max}, over the entire deformation history based on the Ogden and Roxburgh form (Ogden and Roxburgh 1999):

$$\tilde{\eta} = 1 - \frac{1}{r} erf\left(\frac{U_{max} - U}{m + \beta U_{max}}\right) \tag{5}$$

where $\mathrm{erf}(x)$ is the error function and r, β, m are material parameters which dictate the degree of damage and associated hysteresis (Simulia 2013, Mohammed P. Afandi, Wanigasooriya et al. 2017, Wang and Chester 2017); this only influences the unloading-reloading behaviour i.e. no stress softening occurs for monotonic straining and/or constant strain.

The Mullins effect is typical in filled rubbers, where the extent of filler-matrix de-bonding and other damage mechanisms depend upon the level of previously applied maximum strain and leads to reduction in global stress. The Mullins damage model however has also found applicability in predicting the unloading hysteretic large strain behaviour of unleavened bread dough during extrusion (Mohammed P. Afandi, Wanigasooriya et al. 2017). This model is also relevant here due to the presence of fibrous fillers within the starch matrix, as well as due to a micro-cracking damage mechanism which is found to evolve with strain, similar to the Mullins effect (to be shown later in section 4.1).

3.2 Viscoplastic-damage model

3.2.1 Viscoplastic behaviour

In contrast to hyperviscoelasticity, the viscoplastic response implies rate dependent inelastic effects, such that beyond a yield onset stress, σ_{y0}, plastic strains also evolve alongside elastic and viscous/creep strains (Bergstrom 2015). However, in the commercially available FE software the inclusion of viscous/creep strain components within a viscoplastic law typically compromises its compatibility with an additional damage law (Simulia 2013); thus these are assumed to be zero which implies a linear rate independent unloading response with slope equal to the elastic modulus, E. The loading response here consists of a small initial purely elastic regime based on E, followed by a Mises rate dependent plastic behaviour. A similar viscoplastic approach was used by Mohammed et al (Mohammed, Tarleton et al. 2013) in modelling the constitutive response of starch contained in bread dough. The latter however was only calibrated based on compression data and thus did not account for pressure (stress state) dependency. Furthermore, it was not coupled with a damage law to model fracture. The innovation aspect here is the incorporation of both damage and pressure dependency which accounts for different $\sigma - \varepsilon$ plastic behaviour between compression and tension. This was possible by introducing the stress triaxiality parameter, η, parameter within the ABAQUS/Explicit user defined field subroutine, $VUSDFLD$ (Simulia 2013), defined as:

$$\eta = -\frac{p}{\sigma_{eq}} \tag{6}$$

where p and σ_{eq} are pressure and Von Mises/equivalent stress, respectively (Danas and Castañeda 2012, Dunand and Mohr 2014, Lee, Steglich et al. 2017); the uniaxial compression, simple shear and uniaxial tensile states give η = -1/3, η = 0, and η = 1/3, respectively. The law is finally expressed by $\sigma_{eq} = \sigma\left(\varepsilon_{p_{eq}}, \dot{\varepsilon}_{p_{eq}}, \eta\right)$ and is calibrated by providing tabular $\sigma_{eq} - \varepsilon_{p_{eq}}$ test data ($\varepsilon_{p_{eq}}$ is the equivalent plastic strain) for each equivalent plastic strain rate, $\dot{\varepsilon}_{p_{eq}}$, for η = -1/3 (compression) and η = 1/3 (tension); values between the tabular data are computed via linear interpolation during the FE analysis (Simulia 2013). The procedure involves converting the $\sigma - \varepsilon$ test data (Equations (1) and (2)) into $\sigma_{eq} - \varepsilon_{p_{eq}}$ based on decomposition of total equivalent strain, ε_{eq}, into an elastic, $\varepsilon_{e_{eq}}$, and plastic, $\varepsilon_{p_{eq}}$, component (Pyo and Lee 2010, Safaei, Yoon et al. 2014):

$$\varepsilon_{eq} = \varepsilon_{e_{eq}} + \varepsilon_{p_{eq}} \Leftrightarrow \varepsilon_{p_{eq}} = \varepsilon_{eq} - \frac{\sigma_{eq}}{E} \tag{7}$$

while also assuming, $\dot{\varepsilon}_{p_{eq}} \approx \dot{\varepsilon}_{eq}$; this is true only for $E \gg \dot{\sigma}_{eq}$ (via differentiating Equation (7)) which is satisfied here based on a E = 50 MPa used for this material (shown later in section 4.2).

3.2.2 Damage behaviour

In contrast to the Mullins damage effect, the ductile damage law used here degrades the viscoplastic deviatoric stress tensor also under monotonic loading conditions, leading to complete loss of material load carrying capacity i.e. zero stress, which also enables modelling fracture (Simulia 2013). This is shown in Figure 3(a) by a typical viscoplastic-damage model behaviour for a single rate; four distinct parts are specified:

- undamaged viscoplastic regime (a-b-c) based on a yield onset stress, σ_{y0},
- damage onset (c) at an equivalent strain, ε_{eq0},
- damage evolution (c-d) based on surface energy dissipation/fracture toughness, G_c,
- element removal from the calculations once the material stiffness is fully degraded (d).

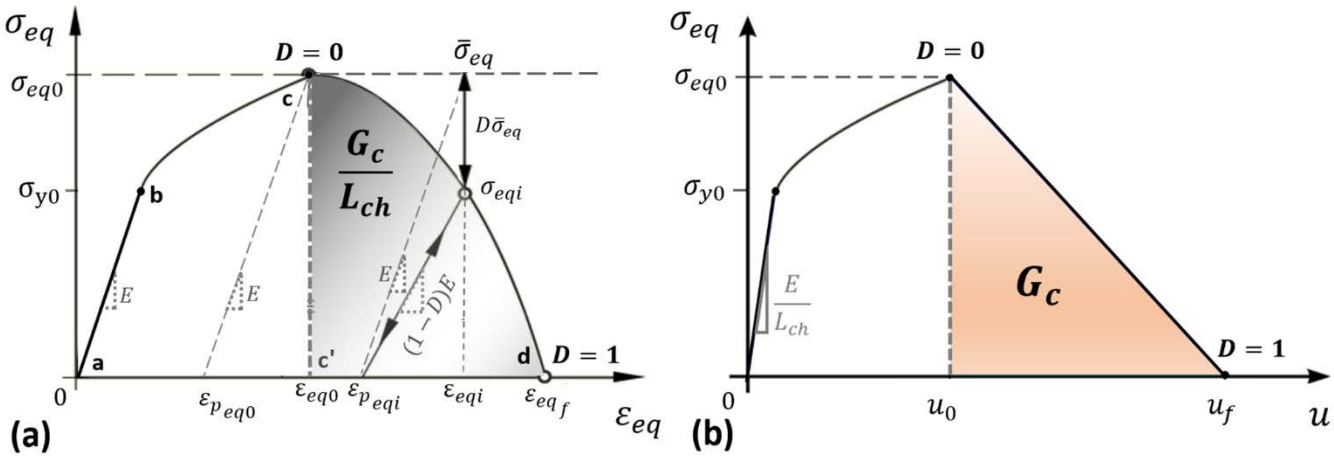

Figure 3. Typical viscoplastic-damage model response for a single element in tension at a single rate; (a) equivalent stress, σ_{eq}, versus equivalent strain, ε_{eq}, response; shaded area represents strain energy density dissipation, U_c (mJ/mm³), discussed in section 4.3.5, (b) corresponding σ_{eq} versus displacement, u, response; shaded area represents G_c (kJ/m²) dissipation.

In Figure 3(a), $\varepsilon_{p_{eq0}}$ is the equivalent plastic strain at damage onset, ε_{eq_f} is the equivalent strain at failure, ε_{eqi}, $\varepsilon_{p_{eqi}}$ and σ_{eqi} are respectively the equivalent strain, plastic equivalent strain and equivalent stress for an arbitrary point of the damage evolution regime, and D is the scalar damage variable. On the other hand, $\bar{\boldsymbol{\sigma}}$ and $\bar{\sigma}_{eq}$ are respectively the effective (fictitious) stress tensor and corresponding effective equivalent stress in the absence of damage, such that during damage (c-d) the respective terms $\boldsymbol{\sigma}$ and σ_{eq} are obtained through:

$$\boldsymbol{\sigma} = (1 - D)\bar{\boldsymbol{\sigma}} \;\Rightarrow\; \sigma_{eq} = (1 - D)\bar{\sigma}_{eq} \tag{8}$$

where D increases from $D = 0$ at the onset of damage, up to $D = 1$ at ultimate element failure. Several hypotheses have been widely adopted in the literature regarding the relation of strain components between the effective and the damaged states. For example, in the absence of plasticity, the strain equivalence hypothesis implies equal strains between the effective and damage states (Cicekli, Voyiadjis et al. 2007, Voyiadjis 2012), although the elastic energy equivalence hypothesis is generally rendered more realistic for describing damage processes e.g. void

nucleation-growth-coalescence or micro-cracking (Voyiadjis and Kattan 1992, Al-Himairee 2011). Nevertheless, here damage evolution is utilised to model macroscopic fracture based on G_c, and thus capturing the details of such damage microstructural mechanisms was not within the scope of this study; also note that the actual relations between the effective and damage state configurations in this material is completely unknown. Consequently, a simple approach is adopted by considering the effective constitutive response (beyond damage onset) perfectly plastic i.e. see constant $\bar{\sigma}_{eq}$ after point 'c' in Figure 3(a). For this condition, investigations through single element simulations of uniaxial tension indicated a common unloading strain, $\varepsilon_{p_{eqi}}$, between unloading from $\overline{\sigma}_{eq}$ and from σ_{eqi}. This implies equal elastic and plastic strains between the effective and damage states.

Instead, a major concern was the comparison of damage based on mesh independent concepts against conventional strain softening damage models. In the latter, damage propagation through adjacent elements by principle depends on the respective element sizes, implying mesh dependency in the results (Simulia 2013, Pack, Luo et al. 2014, Rousselier and Luo 2014, Vignjevic, Djordjevic et al. 2014). This is because total energy dissipation in an element varies with element size for fixed $\sigma_{eq} - \varepsilon_{eq}$ behaviour i.e. energy dissipation decreases as the mesh is refined (smaller elements). Instead, mesh independency is intended here by controlling degradation through the fixed equivalent stress-displacement, $\sigma_{eq} - u$, law (Hillerborg, Modéer et al. 1976) depicted in Figure 3(b), in agreement with the concept of material fracture toughness, G_c (kJ/m²); the latter is equal to the triangular shaded area in Figure 3(b). The displacement, u, is calculated by introducing the characteristic element length, L_{ch}, as a measure of the element size (Lapczyk and Hurtado 2007, Simulia 2013) such that:

$$u = L_{ch}\varepsilon_{eq} \tag{9}$$

G_c is then employed to compute the u at which $D = 1$, notated as u_f (corresponding to ε_{eq_f}), based on:

$$G_c = \int_{\varepsilon_{eq0}}^{\varepsilon_{eqf}} L_{ch}\sigma_{eq}d\varepsilon_{eq} = \int_{u_0}^{u_f} \sigma_{eq}du \tag{10}$$

Here, for a given G_c and a linear stress degradation behaviour, u_f is calculated by:

$$u_f - u_0 = \frac{2G_c}{\sigma_{eq0}} \tag{11}$$

and finally D is updated via:

$$\dot{D} = \frac{\dot{u}}{u_f - u_0} \tag{12}$$

A G_c of 0.93 kJ/m² is considered here as the true toughness for this material, determined recently (Skamniotis, Kamaludin et al. 2017) based on the Essential work of fracture (EWF) methodology. The latter involved a rigorous determination of the energy dissipated at the vicinity of the crack tip during crack propagation, while verifying that G_c is independent of specimen geometry and size i.e. intrinsic material property. As a result, both the damage evolution law (Equation (11)) defined by G_c, as well as the damage onset criterion defined by the tensile failure strain, $\varepsilon_f(\dot{\varepsilon})$ (will be shown later in this section), are based on well-defined material properties.

The ductile damage law defined in terms of stress-displacement, $\sigma_{eq} - u$, is a new equivalent version of the traditional ductile damage law which has been established based on stress-plastic displacement terms (proof of equivalency is provided in the Appendix). It should be also noted that the isotropic damage employed via Equation (8) may not be true here, as crack propagation has been inherently associated with anisotropic softening processes (Ladani and Razmi 2009), particularly in fibre composites (Matzenmiller, Lubliner et al. 1995). In fact, near the crack tip, the material's stiffness may degrade faster in the direction normal to the crack than in the direction of crack propagation, which can only be captured through using a damage tensor instead of the scalar D (Abu Al-Rub and Voyiadjis 2009). However, whether this is indeed the case here was difficult to verify, while no relevant literature exists for this material. Consequently, isotropic damage was judged sufficient for the purposes of this study.

On the other hand, the effect of damage isotropy on the G_c computations was considered. Specifically, based on Equation (11) and for a multi-axial mode of deformation, stress components with negative values (compressive stresses) would still contribute to the equivalent stress σ_{eq} and hence G_c too. The latter is incorrect and may lead to erroneous predictions. Therefore, here the σ_{eq} is replaced by the maximum principal stress, σ_1, and the ε_{eq} is replaced by the maximum principal strain, ε_1, with corresponding values σ_{1_0} and ε_{1_0} at $D = 0$ as well as $\sigma_{1_F} = 0$, ε_F at $D = 1$. This is achieved via the $VUSDFLD$ subroutine in order to define the two field variables, R_σ and R_ε, as shown below:

$$\left.\begin{aligned} (a) \qquad & R_\sigma = \frac{\sigma_{eq0}}{\sigma_{1_0}} \\ (b) \qquad & R_\varepsilon = \frac{\varepsilon_{eq0}}{\varepsilon_{1_0}} = \frac{\varepsilon_{eqf}}{\varepsilon_F} \end{aligned}\right\} \tag{13}$$

as well as to modify the value of G_c into $G_{\check{c}}$ via:

$$G_{\check{c}} = R_\sigma R_\varepsilon G_c \tag{14}$$

where G_c is the fracture toughness in mode I; for a detailed derivation see (Skamniotis, Elliott et al. 2017). Consequently, Equation (14) gives $R_\sigma = R_\varepsilon = 1$, $G_{\check{c}} = G_c = 0.93$ kJ/m² for uniaxial tension ($\eta = 1/3$), and $R_\sigma = \sqrt{3}$, $R_\varepsilon = \frac{2}{\sqrt{3}}$, $G_{\check{c}} \approx 1.82$ kJ/m² for shear ($\eta = 0$), which may be related to fracture toughness in mode II (in-plane shear) (Bárány, Czigány et al. 2010); the experimental determination of mode II toughness in this material was found to be exceedingly challenging due to its highly compliant-dissipative behaviour.

The above development is concerned with damage evolution. Regarding damage onset, the current model allows for various criteria to be specified, such as when ε_{eq0} depends on rate, $\dot{\varepsilon}_{eq}$, and stress state in terms of η (Bai and Wierzbicki 2010, Luo and Wierzbicki 2010, Rousselier and Luo 2014). Previous work in starch (Skamniotis, Patel et al. 2016) indicated that damage and subsequent element deletion for compressive states ($\eta =$ -1/3) led to unreasonable material removal from an FE simulation. However, damage due to shear states ($\eta = 0$) gave accurate fracture predictions in a recent study (Skamniotis, Elliott et al. 2017). Consequently, shear is considered for damage alongside tensile states, leading to $\eta \geq 0$ as a necessary condition for damage onset to occur. The second necessary condition involves comparison of the maximum

principal strain, ε_1, that is encountered in an element against the experimental time/rate dependent tensile failure strain, $\varepsilon_f(\dot{\varepsilon})$, (section 2.2.1), leading to the final damage onset criterion illustrated in Figure 4. This is implemented again via the $VUSDFLD$ subroutine (Simulia 2013) where based on time, t_f, elapsed from the beginning of strain application, $\varepsilon_f(\dot{\varepsilon})$ is updated based on the following empirical form introduced in (Skamniotis, Elliott et al. 2017) which is found to describe well ($R^2 = 0.97$) the tensile test data:

$$\varepsilon_f(\dot{\varepsilon}) = \hat{\mathrm{A}} \ln\left(\int_0^{t_f} \varepsilon \, dt\right) + \mathrm{B} \tag{15}$$

where $\hat{\mathrm{A}}$ (1/s) and B are calibrated material parameters (provided later in Table 2). Equation (15) implies that $\varepsilon_f(\dot{\varepsilon})$ in this material depends upon both the duration and level of strain applied over the entire deformation history.

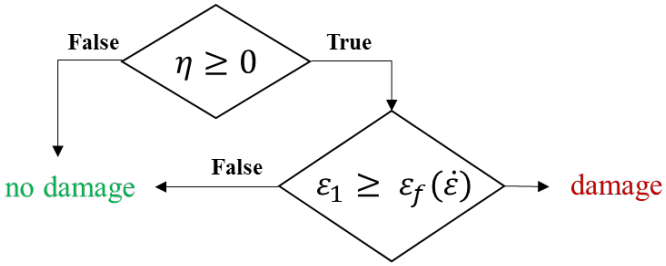

Figure 4. Logical flow diagram of the damage onset criterion.

Importantly, so far the analysis assumed unity element aspect ratios, $\mathcal{A} = 1$, which however is often not the case in FE modelling (Simulia 2013, Skamniotis, Patel et al. 2016). The effect of $\mathcal{A}$ on the damage law computations depends on the L_{ch} calculation method; the one currently available in the literature (Simulia 2013) uses the geometric mean defined as the n^{th} root of the product of n element lengths, L_i:

$$L_{ch} = \left(\prod_{i=1}^{n} L_i\right)^{\frac{1}{n}} = \sqrt[n]{L_1 L_2 \dots L_n} \tag{16}$$

which implies that elements with large $\mathcal{A}$ will exhibit a different damage evolution response. To mitigate this effect, a novel approach is developed here which specifies L_{ch} as a function of element topology and loading direction through the ABAQUS/Explicit $VUCHARLENGTH$ subroutine (Simulia 2013). Specifically, the element dimension that undergoes the maximum tensile strain is identified and then used as the correct L_{ch} in Equation (9), on the basis that G_c dissipation is driven by tensile strains.

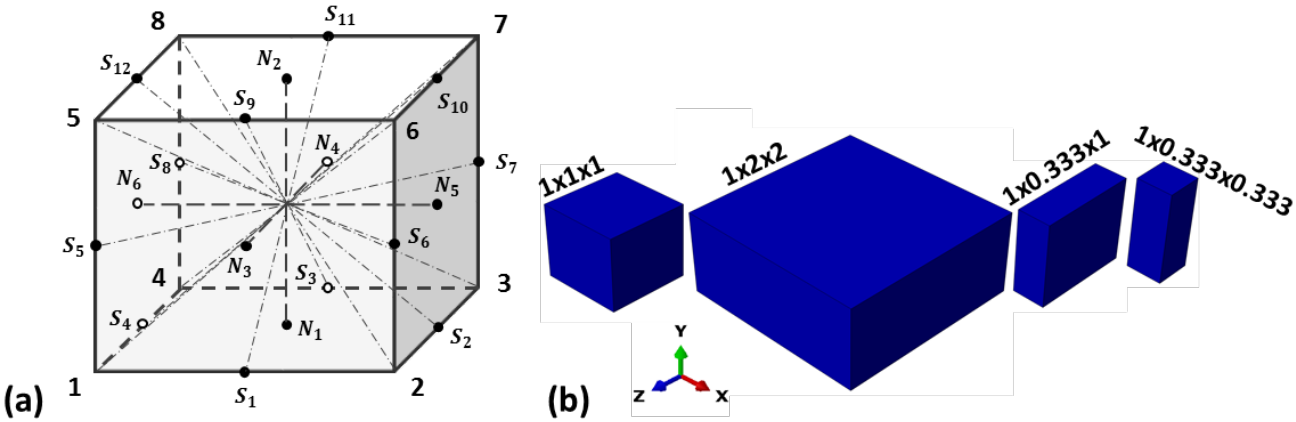

Figure 5. (a) Typical 3D eight-node element; dashed lines denote the thirteen lengths monitored to define L_{ch} via the novel method, (b) four element aspect ratios used to compare the currently available and novel L_{ch} calculation methods.

The method is illustrated in Figure 5(a) through a typical 3D, 8-node element alongside the following thirteen element lengths, L_i, monitored: $L_{S_1S_{11}}$, $L_{S_2S_{12}}$, $L_{S_3S_9}$, $L_{S_4S_{10}}$, $L_{S_5S_7}$, $L_{S_6S_8}$ (across midpoints of parallel edges), L_{17}, L_{28}, L_{35}, L_{46} (diagonals), $L_{N_1N_2}$, $L_{N_3N_4}$, $L_{N_5N_6}$ (across centres of opposite faces); the coordinates of centres of faces and midpoints of edges are computed based on known nodal coordinates during the FE analysis. The use of a total of thirteen L_i is proposed here to account for the unknown direction of the tensile strains relative to the orientation of each element during an FE analysis. This involves calculation of the L_i at the beginning of the analysis ($t = 0$) and when damage onset occurs ($t = t_0$) in order to identify the length associated with the maximum nominal tensile strain, $\varepsilon_{i_{max}}$, given by:

$$\varepsilon_{i_{max}} = \max\left\langle \frac{L_{i_{t=t_0}} - L_{i_{t=0}}}{L_{i_{t=0}}} \right\rangle \tag{17}$$

Thereafter, the original value of the identified length is assigned to the characteristic element length ($L_{ch} = L_{i_{t=0}}$) and is kept constant until element deletion.

The merits of this novel technique are examined via tensile tests on four elements with different $\mathcal{A}$, as shown in Figure 5(b), yet with a common height, $L_{N_1N_2} = 1$ mm, along which $\dot{\varepsilon} = 1$/s is applied. The viscoplastic-damage model calibrated for this material is used based on $G_c = 0.93$ kJ/m², while comparison is drawn between the novel (Equation (17)) and currently available L_{ch} (Equation (16)) calculation results. The following section describes the experimental and model calibration results.

4 Results and discussion

4.1 Uniaxial test data

The average monotonic and loading-unloading experimental $\sigma - \varepsilon$ curves are reported in Figures 6 and 7, respectively, together with the hyperviscoelastic-Mullins, hyperviscoelastic (without Mullins) and viscoplastic-damage model fit. Figure 8 indicates the average experimental unloading as well as permanent strains measured after recovery i.e. two minutes after each test repeat; further recovery after two minutes is negligible. A maximum variability of 9% is found amongst all the average stresses computed from each curve in the experimental data set.

Strong rate dependency is seen both in the $\sigma - \varepsilon$ response and tensile failure strain, ε_f; the latter corresponds to the last data points of the plots in Figure 6(b) which all satisfy Equation (15) based on $\hat{A}$ = -0.024/s and $\mathcal{B} = 0.2$ calibrated values (Skamniotis, Elliott et al. 2017). Each data point for the strain rate, $\dot{\varepsilon} = 0$/s, in monotonic compression and tension corresponds to the equilibrium (long term) relaxation stress (last data point) at the respective constant strain. The monotonic compression curves (i.e. Figure 6(a)) are plotted until the points where the $\sigma - \varepsilon$ calculations are no longer valid since the applied strains are no longer uniform and/or uniaxial. This happens here when specimen barrelling combined with macro-cracking phenomena initiate, as demonstrated in Figure 9(b) for $\dot{\varepsilon} = 0.01$/s. The onset of these effects and the respective data points are a function of rate, which of course relates to the time dependent tensile failure strain, ε_f. Notwithstanding, the time dependency of ε_f is attributed to the formation of micro-cracks normal to the tensile strain direction, as displayed in Figures 10(a-b). Specifically, based on previous work (Skamniotis, Kamaludin et al. 2017) it is suggested that also here micro-cracks evolve with time even when the maximum applied strain is constant, promoting ultimate fracture in the form of a macro-crack (see Figures 9(b) and 10(a) for compression and tension respectively). This can be seen here through the *in-situ* SEM compression images in Figures 9(c) and 9(d) where the micro-cracks are clearly normal to the lateral tensile strain; the latter is caused by the sample's lateral expansion (Poisson's ratio, $\nu = 0.5$).

Micro-cracking likely plays an important role in the non-linearity of the $\sigma - \varepsilon$ curves both in compression and tension, as it theoretically causes loss of load carrying capacity, progressively decreasing the material stiffness with increasing strain. The mechanism is potentially triggered by the progressive de-bonding of fibre-matrix interfaces across the specimen volume with increasing applied strain, as shown in Figure 10(c). This is supported by recent work of the authors in extruded starch (Skamniotis, Patel et al. 2018), where significant fibre pull-out was observed under SEM after fracture, suggesting weak fibre-starch interfacial bonding. The latter suggests strong relevance to the Mullins effect, adding credibility to the Mullins damage model used to capture the unloading response (discussed later in section 4.2). Moreover, since a plastic yielding mechanism is not obvious here, it appears that micro-cracking also contributes majorly to the permanent/plastic strains indicated in Figure 8. A similar phenomenon has been found in biopolymer gel composites in (Plucknett and Normand 2000), where the material was characterised as 'pseudo-plastic'. Figure 8 shows that tension is less prone to plastic deformation than compression, since on average it gives a 0.07 ratio of plastic strain over corresponding maximum applied strain as compared to a 0.25 in compression (compare Figures 8(a) and 8(b)). This suggests that the fibre-matrix de-bonding (see Figure 10(c)) mechanism may evolve differently between compressive and tensile straining, in agreement with previous work on soft tissues (Holzapfel 2001). The latter showed

that fibre stiffening mechanisms are likely inactive in compression, which also here explains the significantly higher stresses in tension than in compression for common absolute strain (compare Figures 6(a) and 6(b)).

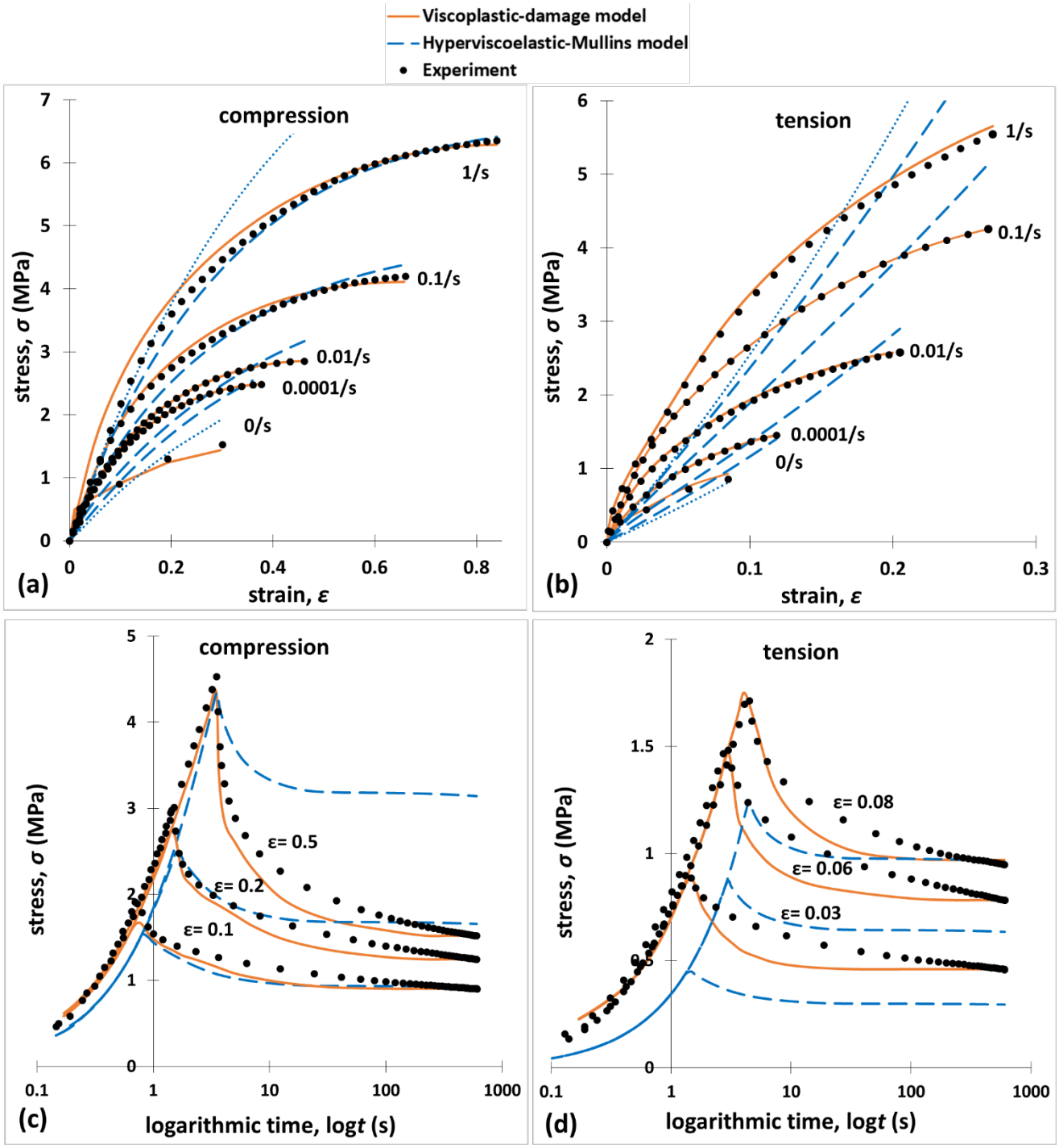

Figure 6. Experimental-model fit results for the hyperviscoelastic-Mullins and viscoplastic-damage models: (a) monotonic compression, (b) monotonic tension, (c) stress relaxation in compression, (d) stress relaxation in tension; the corresponding material model parameters are shown in Tables 1 and 2. In Figures 6(a-b) the upper and lower dotted curves in Figures 6(a-b) represent the instantaneous and long term hyperviscoelastic-Mullins model predictions for extremely high and low rates i.e. 10^{5}/s and 10^{-5}/s, respectively, while the experimental data for 0/s rate correspond to the equilibrium (long term) relaxation stress at the respective constant strain.

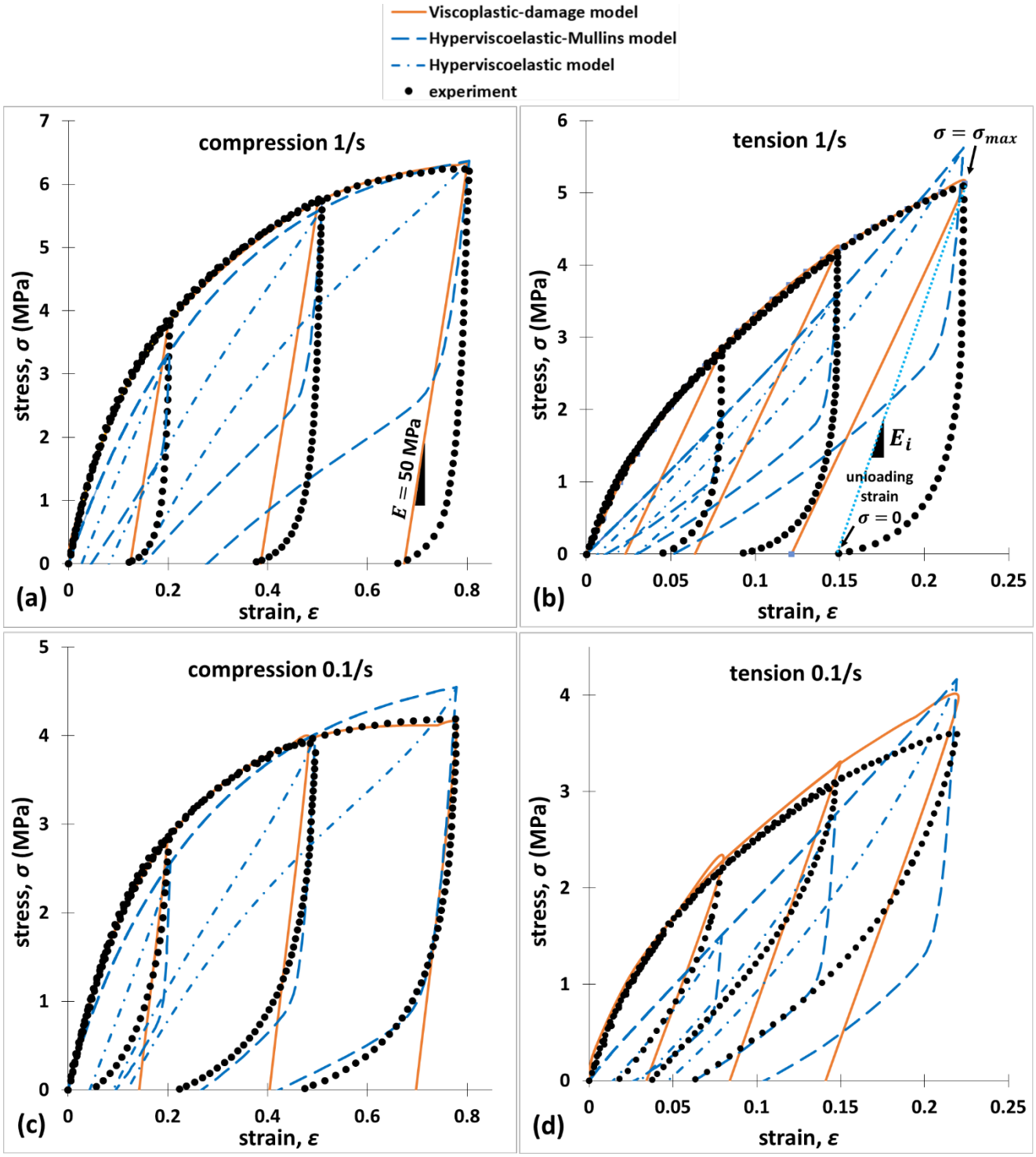

Figure 7. Loading-unloading experimental-model fit results for the hyperviscoelastic-Mullins, hyperviscoelastic without Mullins (dashed plots) and viscoplastic-damage models at two rates and three maximum strain levels: (a) compression at 1/s, (b) tension at 1/s, (c) compression at 0.1/s, (d) tension at 0.1/s; the slope E_i in Figure 7(b) shows the calculation method of the elastic modulus $E = 50$ MPa used in the viscoplastic-damage model, as an average between all the unloading curves.

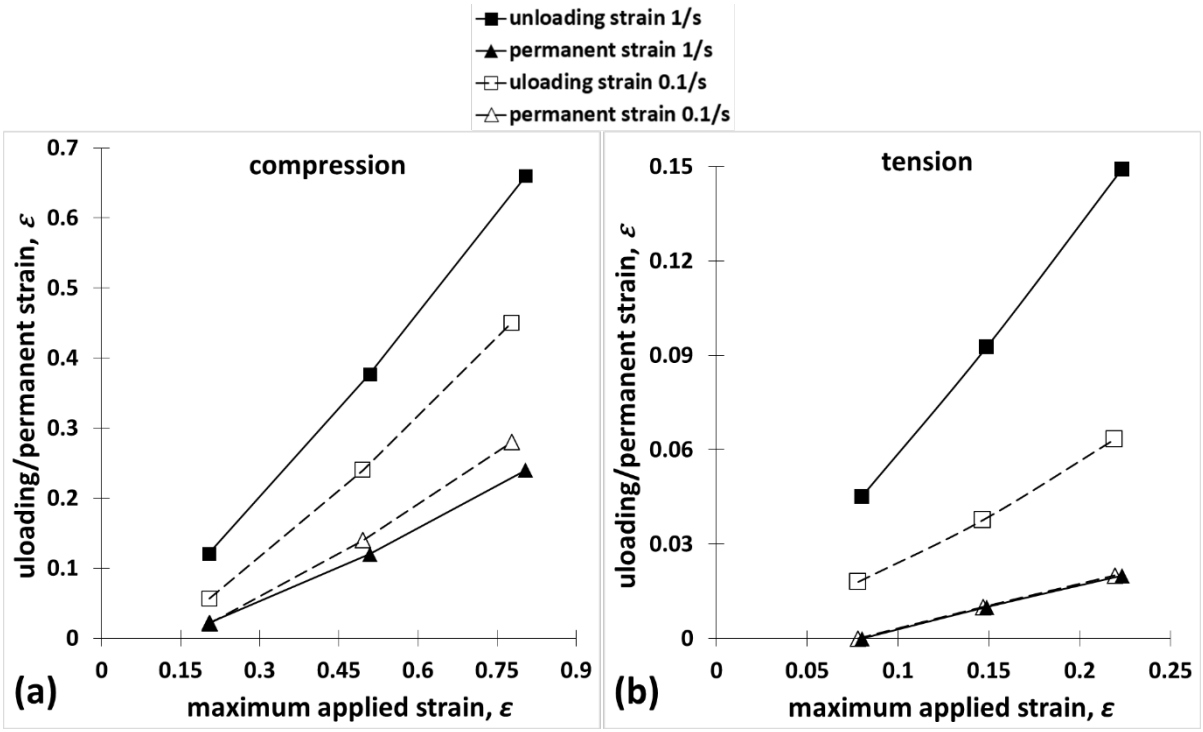

Figure 8. Unloading and permanent/plastic strains as a function of maximum applied strain corresponding to the data plotted in Figure 7; (a) compression (b) tension; unloading strain is defined through the arrow indicated in Figure 7(a).

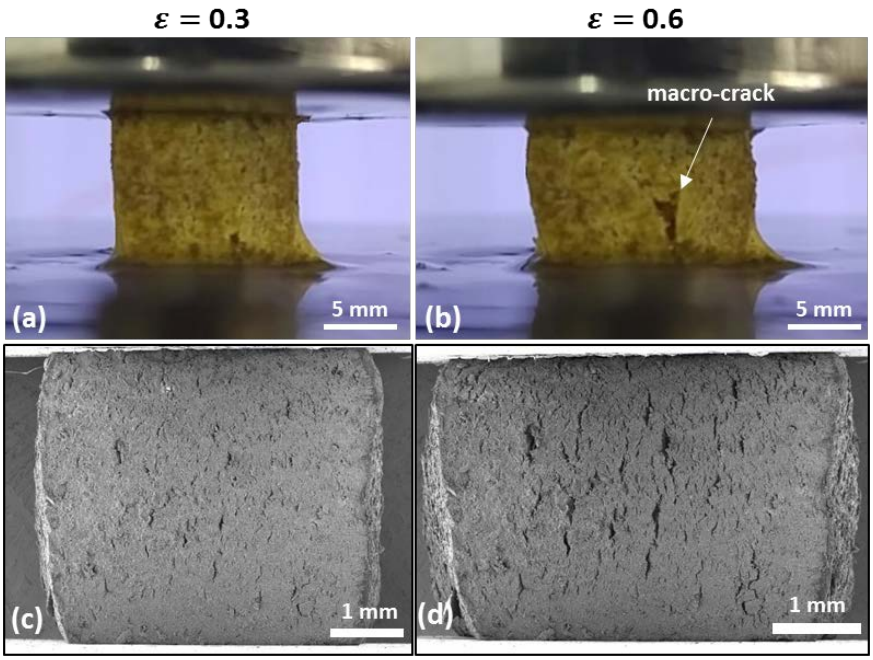

Figure 9. Material behaviour during uniaxial compression: (a) uniaxial compression at $\dot{\varepsilon} = 0.01$/s rate with specimen deformed at $\varepsilon = 0.3$ strain, and in (b) deformed at $\varepsilon = 0.6$ strain showing barrelling and failure through a macro-crack; (c) *in-situ* SEM compression at $\dot{\varepsilon} = 0.01$/s with visible micro-cracking at $\varepsilon = 0.3$ and (d) excessive micro-cracking at $\varepsilon = 0.6$. The frames reveal that the micro-cracks develop normal to the specimen lateral expansion along which tensile strains are induced.

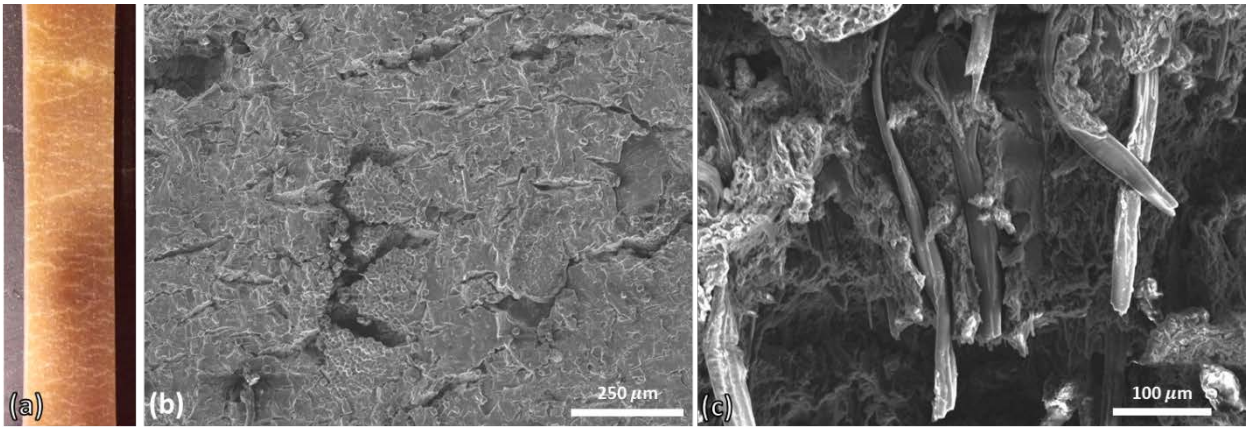

Figure 10. Material behaviour under uniaxial tension: (a) excessive micro-cracking along the gauge length of a fractured specimen – fracture occurred through the indicated macro-crack, (b) micro-cracking under SEM on the same specimen, (c) fibre pull-out and fibre breakage mechanisms detected through SEM imaging of one of the two fractured faces of the specimen in Figures 2(a-b).

Table 1. Calibrated material constants for the hyperviscoelastic-Mullins model based on the Ogden (2nd order) hyperelastic function and Ogden-Roxburgh form for the Mullins damage effect.

Strain dependent parameters - Ogden hyperelastic potential				**Mullins damage parameters**			**Time dependent parameters - Prony series**									
				r	β	m (mJ)	g_1	g_2	g_3	g_4	g_5	g_∞	τ_1 (s)	τ_2 (s)	τ_3 (s)	τ_4 (s)	τ_5 (s)
μ_1 (MPa)	μ_2 (MPa)	α_1	α_2														
41.2	-33.5	0.84	0.1	1	0.1	0	0.05	0.13	0.27	0.09	0.08	0.38	0.09	0.13	1.1	5.5	7000

Table 2. Material constants for the viscoplastic-damage model based on the strain rate and pressure dependent viscoplastic law enhanced by the ductile damage law.

Elastic parameters		**Viscoplastic parameters**				**Ductile damage parameters**	
E (MPa)	ν	σ_{eq} (MPa)	$\varepsilon_{p_{eq}}$	$\dot{\varepsilon}_{p_{eq}}$ (1/s)	η	**Damage onset**	
50	0.49	0.01,...,1.49	0, 0.01,...,0.68	0	-1/3	Â (1/s)	Ɓ
		0.03,...,2.49	0, 0.01,...,0.68	0.0001	-1/3	-0.024	0.2
		0.05,...,2.61	0, 0.01,...,0.68	0.001	-1/3	**Damage evolution**	
		0.1,...,2.86	0, 0.01,...,0.68	0.01	-1/3	G_c (kJ/m^2)	f
		0.2,...,4.2	0, 0.01,...,0.68	0.1	-1/3	0.465	0
		0.25,..., 6.37	0, 0.01,...,0.68	1	-1/3	0	1
		0.004,...,1.02	0, 0.01,...,0.68	0	1/3		
		0.05,...,1.45	0, 0.01,...,0.68	0.0001	1/3		
		0.1,...,1.79	0, 0.01,...,0.68	0.001	1/3		
		0.2,...,2.57	0, 0.01,...,0.68	0.01	1/3		
		0.5,...,4.26	0, 0.01,...,0.68	0.1	1/3		
		0.9,...,5.65	0, 0.01,...,0.68	1	1/3		

4.2 Constitutive law fits

The $\sigma - \varepsilon$ predictions plotted in Figures 6 and 7 correspond to the calibrated parameters shown in Table 1 for the hyperviscoelastic-Mullins and hyperviscoelastic (without Mullins), as well as in Table 2 for the viscoplastic-damage model. The hyperviscoelastic-Mullins model predicts compression reasonably well, yet disagreement is found for relaxation at the large compressive strain, $\varepsilon = 0.5$ (Figure 6(c). This is because the model lacks in capturing irreversible effects such as material stiffness degradation at constant strain and plastic deformation; note that Figure 8(a) indicates a permanent strain of approximately 0.12 for $\varepsilon = 0.5$ maximum applied strain. Notably, although the Mullins effect is intended for modelling softening, yet it is effective only during unloading.

The major compromise, on the other hand, associated with the hypervisoelastic-Mullins model is the tensile response which in reality is significantly stiffer with a larger degree of non-linearity (see Figures 6(b) and 6(b)). Despite rigorous calibration efforts including different hyperelastic functions, it was found impossible to fit accurately both compression and tension simultaneously. Although hyperelastic functions do predict higher stresses in tension than in compression for the same absolute strain (Destrade, Murphy et al. 2013), this effect is magnified in the starch studied here, potentially due the fibre stiffening effect being inactive in compression causing a steep or even discontinuous increase in the material stiffness as the deformation state changes from compression into tension. This imposes considerable numerical complexities in that a unique hyperelastic potential that accounts for the above sharp transition is difficult to obtain and of course has not been yet considered in any of the hyperelastic potentials developed in this field. As a matter of fact, for this material, in order to achieve accurate fits for compression, the tensile predictions need to be compromised and vice versa. Due to the above reasons, extending the hyperelastic-Mullins model in order to include plasticity was not considered. For example, employing advanced models for non-linear viscoelasticity, such as the recently developed Parallel Rheological Framework (PRF) (Hurtado, Lapczyk et al. 2013), are expected to capture accurately the large strain ($\varepsilon = 0.5$) relaxation response (Figure 6(c)), as well as generally improve the unloading fit (fit discussed later via Figure 7) in these materials. However, a new hyperelastic potential would still be required to account for the sharp transition in material stiffness between compression and tension, which is mainly responsible for the experimental-model discrepancy here (Figure 6).

Regarding loading-unloading, the hyperviscoelastic-Mullins model shows some merits especially in Figure 7(c) for $\dot{\varepsilon} = 0.1$/s, although the quality of the fit degrades for $\dot{\varepsilon} = 1$/s by underestimating the amount of hysteresis, especially when the Mullins effect is excluded (dashed plots). Efforts to tackle this involved reducing β to very low values i.e. $\beta = 10^{-4}$, maximising the possible amount of hysteresis (Bergstrom 2015). However, for $\beta < 0.1$ the fit did not improve further, while a $\beta = 10^{-4}$ caused convergence problems in single element tensile simulations; this owes to a discontinuous change in the slope/material stiffness during unloading (Simulia 2013).

In contrast, the above limitations are no longer a concern in the viscoplastic-damage model. Its supremacy over the hyperviscoelastic-Mullins model is demonstrated by the excellent fit shown in Figure 6. The almost exact reproduction of the monotonic response implies that the condition $\dot{\varepsilon}_{p_{eq}} \approx \dot{\varepsilon}_{eq}$ (section 3.2.1) is satisfied, while the long term stresses are also exactly captured via specifying the experimental long term stresses as the σ_{eq} data for the $\dot{\varepsilon}_{p_{eq}} = 0$/s rates in Table 2.

Reasonable unloading predictions are also obtained, with the ones for uniaxial tension being less accurate than these for compression (compare Figures 7(a) and (c) with 7(b) and (d)). This is

because a common modulus, E, is used while the material is stiffer in tension than in compression. Efforts to also specify E as a function of η involved using $E = 40$ MPa in compression and $E = 60$ MPa in tension; these were calculated by the slopes between the points at onset of unloading (when $\sigma = \sigma_{max}$) and the points at the end of unloading (when $\sigma = 0$) as denoted in Figure 7(a), on average over all the loading-unloading curves, for compression and tension, respectively. Although this was successfully implemented in single element simulations, this was not the case in larger models involving multiaxial stress states i.e. spherical indentation, where convergence problems occurred. This owes to a continuously varying η with increasing strain of a material point leading to continuous changes of E, which hinders the correct decomposition of the total deformation gradient into an elastic and a plastic gradient (see Equation 7). Consequently, using the average E= 50 MPa between 40 MPa (compression) and 60 MPa (tension) was found to be the best practise for this material here. In cases where the unloading behaviour is critical, the above limitation may be addressed by extending the current viscoplastic-damage model to include a viscous strain component, as for example performed through the advanced two-layer viscoplastic model (Berezvai and Kossa 2017). However, as already mentioned in section 3.2.1, this would compromise the compatibility with additional damage laws in order to model fracture, which is the main scope here.

4.3 Modelling fracture

4.3.1 Fracture experiment and suitability of models

The results of the fracture experiment are shown in Figure 11 in terms of the crack propagation observations while Figure 15 shows the corresponding $F - \delta$ data; these displayed a 7% variation in the area under the $F - \delta$ curves over the five repeats. Although Figure 11(a) shows crack initiation in only one notch, the crack initiation time difference between the two notches was small enough such that the assumption of symmetry for the associated FE model (section 2.3) is valid.

The two material models studied here differ entirely in the way they can be utilised to reproduce the fracture experiment. The hyperviscoelastic-Mullins model mandates the use of special purpose cohesive elements (cohesive zone approach), which undergo damage and finally delete in order to predict crack initiation and propagation based on purely fracture mechanics concepts. A limitation of this approach is that it typically requires previous knowledge of the crack path which is not possible for applications involving multi-axial loads and/or complex geometries are e.g. material forming, food oral breakdown, tooth fracture, puncturing of automotive tyres. In contrast, the viscoplastic-damage here is a stand-alone model in the sense that these cohesive elements are not needed and damage in the form of element deletion can occur in any element of the FE mesh based on a combination of damage mechanics and fracture mechanics concepts. Conclusively, the following analysis is performed for the viscoplastic-damage model.

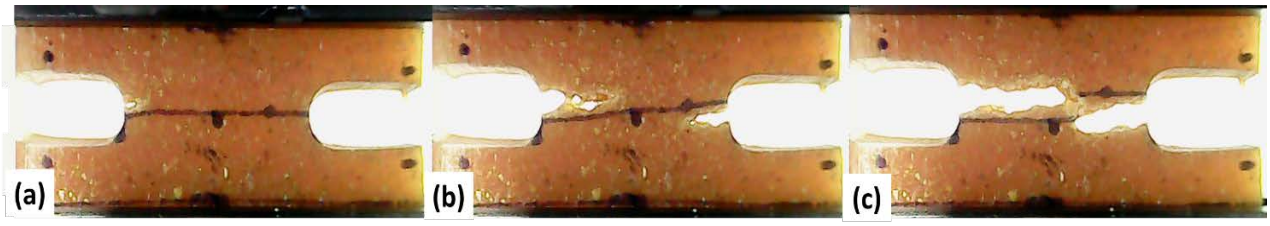

Figure 11. Video frames of the fracture experiment; (a) fracture initiation (left notch), (b) instance during fracture propagation either side, (c) end of test – final specimen separation.

4.3.2 Effect of element aspect ratio on the stress softening response

Prior to the application of the viscoplastic-damage model in fracture simulations (section 2.3), mesh dependency results in terms of element aspect ratio, $\mathcal{A}$, effects on the stress softening response are here examined for the first time. Based on the method described in section 3.2.3 and the viscoplastic-damage model parameters summarised in Table 2, Figures 12(a) and 12(b) show the deformed state just before deletion i.e. $D = 0.99$ of the four elements, according to the novel (Equation 17) and current (Equation 16) L_{ch} calculation, respectively; the corresponding $\sigma - \varepsilon$ results are plotted in Figures 12(c) and 12(d). Clearly, Figures 12(a) and 12(c) demonstrate a consistent response (elements stretch to the same height at $D = 0.99$) and thus correct dissipation of $G_c = 0.93$ kJ/m² regardless of $\mathcal{A}$, as opposed to Figures 12(b) and 12(d) which demonstrate inconsistent, erroneous amounts of G_c dissipation (values denoted in Figure 12(d)) for $\mathcal{A}$ other than unity (elements stretch at different heights at $D = 0.99$). This owes to Equation (16) giving varying L_{ch} (values denoted in Figure 12(d)), leading to a profound effect of $\mathcal{A}$ on the actual G_c dissipation, despite the fact that a fixed $G_c = 0.93$ kJ/m² is used as input in the material model definition. This shows that correct L_{ch} calculation is in fact critical when using the viscoplastic-damage law, adding credibility to the novel method developed here (section 3.2.3); the latter is thus used in the fracture simulations presented in the following section.

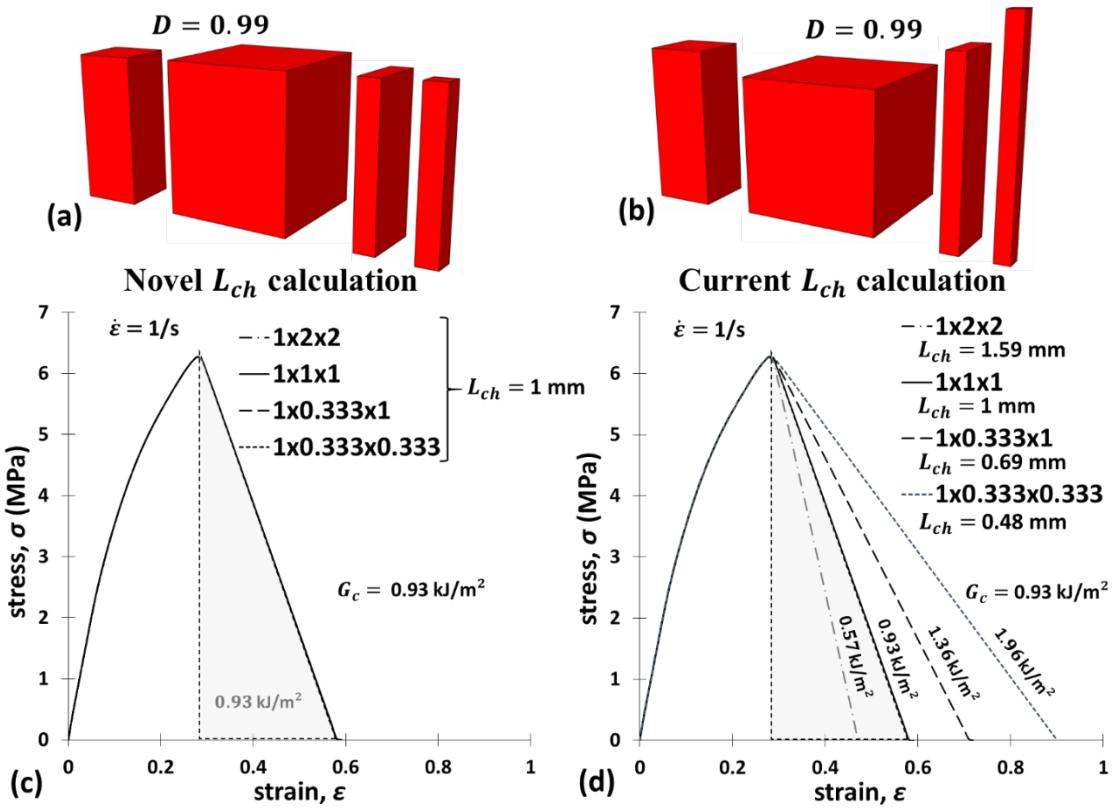

Figure 12. Effect of element aspect ratio, $\mathcal{A}$, on the viscoplastic-damage model response at a single rate, $\dot{\varepsilon} = 1/s$; (a) consistent strain between elements at $D = 0.99$ based on the novel L_{ch} calculation, (b) inconsistent strain between elements at $D = 0.99$ based on the current L_{ch} calculation, (c) consistent $\sigma - \varepsilon$ results and G_c dissipation based on novel L_{ch} calculation, (d) inconsistent $\sigma - \varepsilon$ damage evolution response and G_c dissipation based on current L_{ch} calculation; the actual dissipated energies and L_{ch} calculation results are denoted.

4.3.3 Crack initiation & propagation

Figure 13(a) illustrates the damage variable, D, contour results of the fracture FE model (section 2.3) at maximum applied (global) displacement, $\delta_{max} = 4$ mm; elements of $\mathcal{A} = 1$ are uniformly used in the mesh region '1' (see Figure 2(a)) with edge length of 0.05 mm, implying that also $L_{ch} = 0.05$ mm regardless of using Equation (16) or (17) for the calculation. An extremely ductile behaviour is apparent such that no crack initiation occurs in the form of element deletion. This owes to the blunt notch and the associated low strain concentration, leading to a very large distribution of damage across the specimen bulk (maximum $D = 0.31$ at the notch tip - Figure 13(a)). This conflicts with the concept of damage based on material toughness, G_c, implying that the viscoplastic-damage model in its current version fails to predict the correct fracture behaviour, not least it cannot model crack initiation in this tough material without the presence of an initial sharp crack.

This is addressed through specifying a $G_c = 0$ kJ/m² for the elements of the external notch surface of the mesh region '1' denoted in Figure 2(b), for which a predefined field variable, $f = 1$, is assigned as shown in Table 2 (Simulia 2013); an $f = 0$ condition instead characterises all the other elements of the mesh. This technique implies sudden element deletion as soon as damage onset is met only when $f = 1$, i.e. steep change from $D = 0$ (no damage) to $D = 1$ (full damage). Thus, a crack tip is created just when the tensile failure strain is reached; the latter here occurs first in the elements highlighted in red in Figure 2(b), leading to the behaviour shown in Figure 13(c). Although this may not be physically true, the technique is practically valid since the $G_c = 0$ kJ/m² condition is only applied to the elements at the notch tip surface, which are a tiny fraction of the total mesh, as shown in Figure 13(b).

The concept of G_c based on fracture mechanics principles requires that damage is encountered only along a single layer of elements across the Y-axis i.e. a layer on the symmetry X-Z plane, as it is performed in cohesive zone models. This is not seen by the D contours in Figure 13(c) which reveals that crack propagation numerically manifests itself in the form of two adjacent layers of elements undergoing damage. Therefore, the FE model in fact requires a total dissipation of $2G_c = 1.86$ kJ/m² to drive crack propagation, in contrast to the true material toughness, $G_c = 0.93$ kJ/m². This was tackled via using a toughness parameter reduced by a factor of two i.e. inputting 0.465 kJ/m² in Table 2. Note that the latter does not contradict with the experimentally determined material parameter, $G_c = 0.93$ kJ/m². Instead, the reduced parameter serves in obtaining agreement between the concept of fracture toughness and its numerical implementation by the viscoplastic-damage model.

Indeed upon application of the above modifications and for $L_{ch} = 0.05$ mm in the mesh region '1' (Figure 2(b)), a close experimental-model agreement is obtained both in terms of the fracture patterns depicted in Figure 14, as well as in terms of the $F - \delta$ data reported in Figure 15(a); the I, II and III frames of Figure 14 (see caption) correspond to the data points indicated in Figure 15(a). This adds credibility to the modified implementation of the viscoplastic-damage as a powerful but also a convenient solution in studying various complex physical processes in highly non-linear materials.

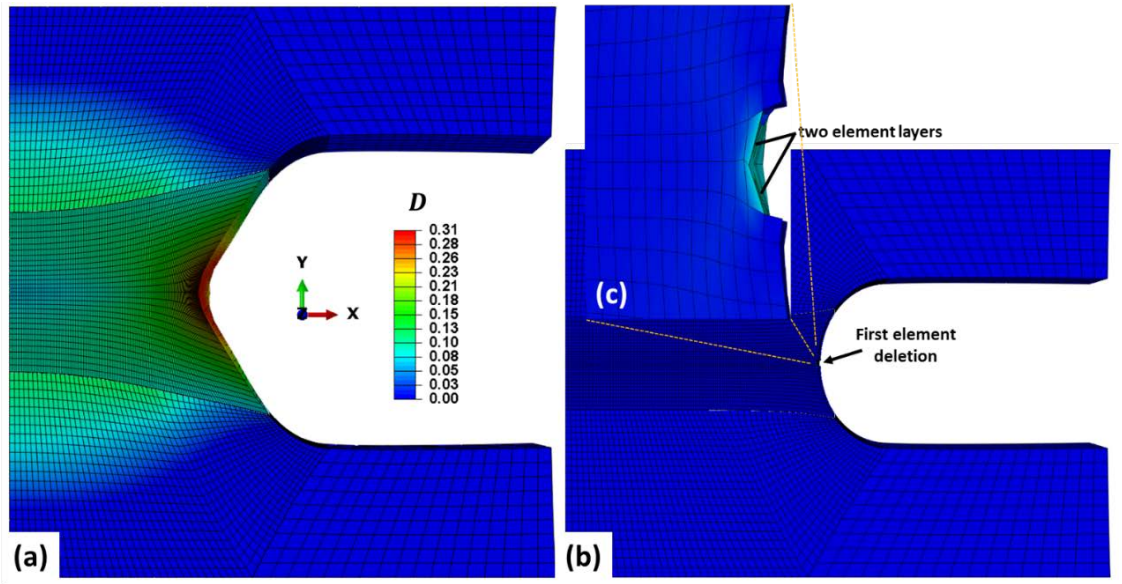

Figure 13. FE model results in terms of damage variable, D, contours when: (a) $G_c = 0.93$ kJ/m² is specified in all the elements of the model - frame corresponds to maximum displacement $\delta_{max} = 4$ mm, (b) $G_c = 0$ kJ/m² is specified in the elements of the notch tip surface and $G_c = 0.93$ kJ/m² defined in all the other elements - frame corresponds to instance of first element deletion/crack initiation while the crack tip detail is depicted in image (c).

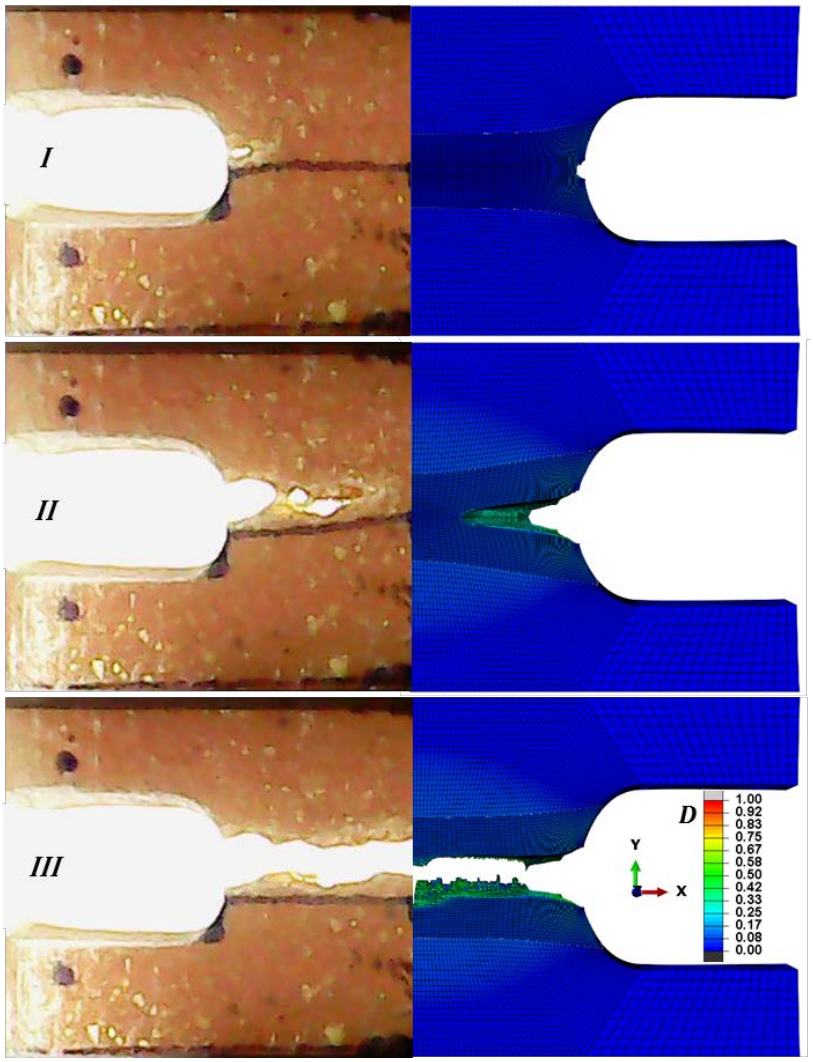

Figure 14. Comparison of crack initiation and propagation behaviour (D contours) between experiment (left)-FE model (right) when the modified ductile damage law is used; results correspond to uniform element size and aspect ratio based on L_{ch} = 0.05 mm and $\mathcal{A}$ =1 in the fine mesh region. Frames I and II correspond to primary and late stage of crack propagation while III corresponds to ultimate specimen separation.

4.3.4 Effect of element size on fracture behaviour

The element size effect is studied through preserving the element aspect ratios at $\mathcal{A} = 1$ while varying the edge length (equal to L_{ch} for $\mathcal{A} = 1$ based on either Equation (16) or (17)) between 0.02, 0.05, 0.1, 0.15 and 0.2 mm uniformly in mesh region '1' (see Figure 2(a)). The $\mathcal{A} = 1$ condition is chosen to avoid undesirable effects of $\mathcal{A}$ on the level of mesh distortion at the crack tip; the latter is described below. Interestingly, despite the theoretically mesh independent concept of the damage law (section 3.2.2), in fact Figure 15(a) displays strong mesh dependency in terms of L_{ch} on the $F - \delta$ response, such that the latter does not approximate the true (experimental) $F - \delta$ behaviour with mesh refinement i.e. towards $L_{ch} = 0.02$ mm. Figure 15(a) includes the $F - \delta$ response for $G_c = 0$ kJ/m² and $L_{ch} = 0.05$ mm which is plotted to represent the perfectly brittle fracture and to indicate the point of crack initiation (first element deletion). The latter is found to occur at the same δ amongst all the L_{ch} used, implying that crack initiation is clearly mesh independent in the L_{ch} studied here and instead depends only on the damage onset criterion through Equation (15). Consequently, mesh sensitivity in Figure 15(a) is induced only through the dependency of the viscoplastic-damage model crack propagation behaviour on L_{ch}.

Indeed, this is demonstrated through Figures 16(a-d) where for a common applied (global) displacement, $\delta = 2$ mm, a $L_{ch} = 0.1$ mm leads to significantly less deformation around the crack tip (see crack tip detail in Figure 16(d)) compared to $L_{ch} = 0.02$ mm which leads to no crack propagation at all (see crack tip detail in 16(b)); in the latter the FE analysis aborted at $\delta = 5$ mm due to excessive element distortion. Based on Equation (10), a brittle response for large elements is expected, since larger L_{ch} implies small strains required for G_c dissipation, and consequently, small strains beyond damage onset. For example, for the extreme case of $L_{ch} = 0.2$ mm, the element state was found to change quickly from undamaged to fully damaged, such that one or two elements ahead of the crack tip were only simultaneously undergoing damage. Therefore, it appears that the stress-displacement, $\sigma - u$, law alone, does not suffice to model the true fracture behaviour since consistent $\sigma - u$ between varying L_{ch} implies different strain levels in the stress-softening/damage evolution regime. Depending on these strain levels, a markedly different strain field develops in the crack tip region. This region can be considered equivalent to the numerical fracture process zone/region (FPZ), commonly taken into account when modelling fracture via the cohesive traction-separation law (Sarrado, Leone et al. 2014). Specifically, the current practise is to ensure that at least several elements (five to ten) are always in the FPZ i.e. several elements simultaneously undergo damage, the exact element number being empirical. This is satisfied here for $L_{ch} \leq 0.05$ mm which explains why the fracture resistance is underpredicted for $L_{ch} > 0.05$ mm (Figures 16(c-d) and 15(a)).

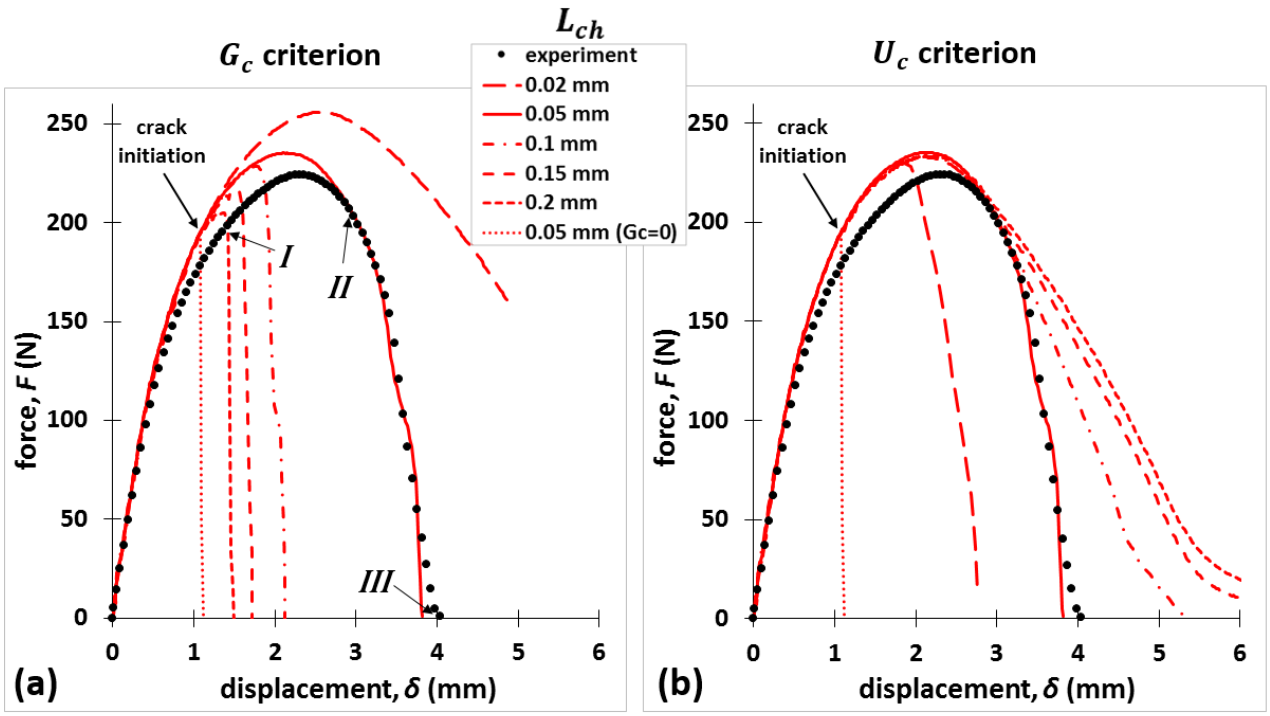

Figure 15. Comparison of experimental-model $F - \delta$ response for five element sizes/lengths, L_{ch}, used in the fine mesh region: 0.02, 0.05, 0.1, 0.15, 0.2 mm, and between using two energy dissipation criteria: (a) G_c criterion and (b) U_c criterion; the behaviour for $G_c = 0$ kJ/m² is also predicted.

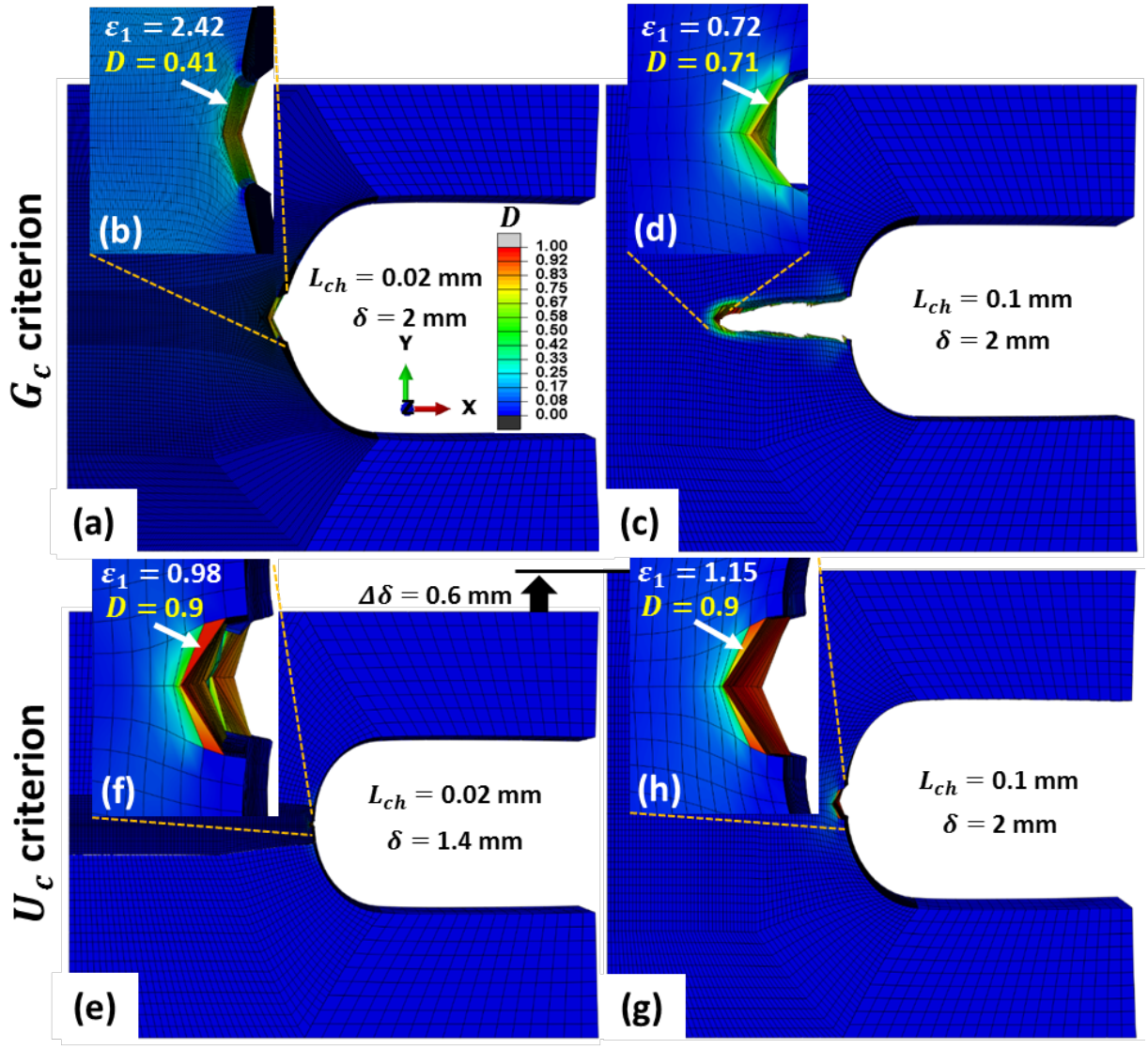

Figure 16. Comparison of fracture behaviour together with crack tip details between using the $G_c$and U_c dissipation criteria, each implemented in two different mesh densities in terms of L_{ch}: (a-b) G_c criterion for $L_{ch} = 0.02$ mm, (c-d) G_c criterion for $L_{ch} = 0.1$ mm, (e-f) U_c criterion for $L_{ch} = 0.02$ mm, (g-h) U_c criterion for $L_{ch} = 0.1$ mm; the (a-d) frames are compared for a consistent $\delta = 2$ mm whereas the (e-h) frames correspond to a common maximum $D = 0.9$.

On the other hand, mesh refinement through $L_{ch} < 0.05$ mm is typically expected to improve accuracy, which is not true here for $L_{ch} = 0.02$ mm (see Figures 16(a-b) and 15(a)). This owes to the extremely large strains required by very small elements in order to reach the displacement essential for G_c dissipation, u_f (Equation 10). Indeed, Figure 16(b) shows excessive crack tip blunting, with a maximum principal strain of $\varepsilon_1 = 2.42$ while still $D = 0.41$. These effects worsen with further mesh refinement, which explains why the results do not approximate the true $F - \delta$ behaviour determined experimentally (Figure 15(a)). Conclusively, although the current damage model theoretically incorporates a material length scale through a combination of the L_{ch} and G_c concepts, yet numerical aspects related to mesh distorsion at the crack tip do not allow for mesh independent results to be obtained.

4.3.5 Comparison of G_c-softening against strain softening

Further investigations involved comparison of the damage law based on G_c criterion with a corresponding damage law based on strain softening. Since the latter is known to lead to spurious mesh dependency in the results, this investigation examined whether a strain softening law leads to a consistent deformation field near the crack tip i.e. self-similar FPZ. This was performed by modifying the G_c criterion such that varying size elements undergo the same strains during damage evolution i.e. stress-strain, $\sigma_{eq} - \varepsilon_{eq}$, degradation law, giving rise to a strain energy density dissipation, U_c (mJ/mm³), criterion for element deletion, instead of the strain energy release rate, G_c (kJ/m² = mJ/mm²), which is used so far. The U_c is equivalent to the shaded area under the $\sigma_{eq} - \varepsilon_{eq}$ softening response denoted in Figure 3(a), such that:

$$U_c = \frac{G_c}{L_{ch}} \tag{19}$$

which here gives $U_c = 0.465/0.05 = 9.3$ mJ/mm³ for $L_{ch} = 0.05$ mm that matches the experimental fracture data (see Figure 15(a)). The criterion is implemented via the $VUSDFLD$ subroutine by changing G_c between L_{ch}, such that $U_c = 9.3$ mJ/mm³ is always satisfied, implying that for $L_{ch} =$ 0.02, 0.05, 0.1, 0.15, 0.2 mm, the toughness parameter is respectively $G_c = 0.186$, 0.465, 0.93, 1.395, 1.86 kJ/m². Note that in contrast to G_c, the U_c parameter here is not introduced as a material property but instead it is investigated as a numerical correction factor against inconsistent strain fields around the crack tip.

Figure 15(b) depicts the $F - \delta$ response associated with the U_c criterion, which by comparison with Figure 14(a) (G_c criterion) indicates that although the U_c criterion fundamentally implies a mesh dependent G_c dissipation, in fact here reduces mesh dependency with a closer agreement in the maximum force predictions between varying L_{ch}. As expected, the U_c criterion does give consistency in the crack tip deformation field, with a slight difference observed in terms of the maximum principal strain, being $\varepsilon_1 = 0.98$ for $L_{ch} = 0.02$ mm in Figure 16(f), compared to 1.15 for $L_{ch} = 0.1$ mm in Figure 16(h), both corresponding to a common maximum damage variable, $D_{max} \approx 0.9$. However, here the mesh dependent effects of L_{ch} on the results are reversed (see

Figure 15(b)), giving increasing δ for fracture (more ductile response) with increasing L_{ch}. The latter is expected as for increasing L_{ch}, the $\sigma_{eq} - \varepsilon_{eq}$ degradation law implies increasing element displacements, u_f, which in turn lead to increasing FPZ sizes i.e. compare FPZ between Figure 16(e) for $L_{ch} = 0.02$ mm and Figure 16(g) for $L_{ch} = 0.1$ mm. Summarising, for the material studied here it is found that the theoretically mesh independent damage law based on G_c does not show any merits over a conventional mesh dependent strain softening law.

5 Conclusions

Our study provides a comprehensive framework for characterising and modelling the large strain fracture processes of soft bio-composites such as short cellulose fibre reinforced starch extrudates. The latter are characterised and modelled by investigating for the first time the suitability of various theories in predicting their stress-strain and crack propagation response.

For these newly investigated systems, the merits of both the hyperviscoelastic-Mullins damage and viscoplastic-damage models are examined. The hyperviscoelastic-Mullins model captures well time-dependent and highly dissipative characteristics. Yet, it appears that the significantly stronger fibre stiffening effect in tension than in compression as well as the severe stress-strain non-linearity due to micro-cracking cannot be captured through any of the hyperelastic potentials available. In contrast, these phenomena are well predicted by the pressure dependent viscoplastic-damage model, which also predicts fracture by combining continuum damage mechanics and fracture mechanics principles, in a straightforward manner i.e. without specifying the crack path. The latter involves a strict fracture toughness G_c criterion to drive damage evolution and subsequent crack propagation in the form of element deletion.

The credibility of this approach is demonstrated by reproducing closely an independent ultimate fracture experiment on specimens free of pre-existing cracks, based on known experimental G_c values. This replaces the common practice of specifying cohesive zones to predict fracture, whilst also being superior to conventional strain softening local continuum damage models. However, G_c dissipation is revealed highly sensitive to the element aspect ratio, giving erroneous results for large aspect ratios, previously unreported. This is tackled through a novel calculation of the characteristic element length, used in the damage computations, based on the direction of the maximum principal strain and element geometry. On the other hand, although the G_c driven softening model applied here is built upon mesh independent concepts which incorporate a material length scale, i.e. stress degrades as a function of element elongation instead of strain, yet the results do not converge into a true response as the mesh is refined. This owes to small elements requiring unrealistically large strains in order to reach the prescribed element elongation postulated by the G_c criterion, causing mesh distortion phenomena at the crack tip. Instead, larger elements require lower strains and can lead to sudden element deletion and subsequent brittle-like fracture. This suggests that for a known G_c the current approach requires a balance to be found between the above two extremes, giving rise to gradient-enhanced non local damage models as alternative options against mesh dependency.

Our work aims to address the latest computational modelling challenges involved in complex soft bio-composite applications where large deformations, damage and macro-scopic material separation need to be simultaneously predicted. The above findings will drive future research and industrial design in this class of materials for biomedical, food and packaging applications.

Acknowledgements

The authors would like to acknowledge Mars Petcare for the financial support and for providing the samples.

Appendix: Equivalency between the ductile damage law implementation based on total equivalent strain versus based on plastic equivalent strain

The ductile damage law has been originally introduced in the literature through plastic terms, by using the effective plastic displacement, u_p, for which $u_p = 0$ at $D = 0$, (Simulia 2013). This includes the following set of equations:

$$u_p = L_{ch}\left(\varepsilon_{p_{eq}} - \varepsilon_{p_{eq0}}\right) \tag{A1}$$

$$G_c = \int_{\varepsilon_{p_{eq0}}}^{\varepsilon_{p_{eqf}}} L_{ch}\sigma_{eq}\, d\varepsilon_{p_{eq}} = \int_0^{u_{pf}} \sigma_{eq}\, du_p \tag{A2}$$

$$u_{pf} = \frac{2G_c}{\sigma_{eq0}} \tag{A3}$$

$$D = \frac{u_p}{u_{pf}} \tag{A4}$$

where u_{pf} is the effective plastic displacement at element deletion. Regardless of using u or u_p, here it is shown that Equations (11) and (A2) are equivalent when the constitutive behaviour in the absence of damage is perfectly plastic beyond damage onset i.e. see constant $\bar{\sigma}_{eq}$ after point 'c' in Figure 3(a). This is because based on Equation (9) the latter condition implies:

$$\sigma_{eqi} = (1 - D)\sigma_{eq0} \tag{A5}$$

while by performing strain decomposition (Equation (8)) at damage onset ($\sigma_{eq} = \sigma_{eq0}$) and at an arbitrary point ($\sigma_{eq} = \sigma_{eqi}$) in the stress softening regime (see Figure 3(a)), it is deduced that:

$$\varepsilon_{p_{eq0}} = \varepsilon_{eq0} - \sigma_{eq0}/E \tag{A6}$$

and

$$\varepsilon_{p_{eqi}} = \varepsilon_{eqi} - \frac{\sigma_{eqi}}{(1-D)E} \qquad (A7)$$

Finally, by subtracting Equation (A6) from (A7) and via considering Equation (A5), it is deduced that:

$$\varepsilon_{p_{eqi}} - \varepsilon_{p_{eq0}} = \varepsilon_{eqi} - \varepsilon_{eq0} \qquad (A8)$$

proving equivalency between Equations (10) and (A2).

References

1. Abendroth, M. and M. Kuna (2006). "Identification of ductile damage and fracture parameters from the small punch test using neural networks." Engineering fracture mechanics **73**(6): 710-725.
2. Abu Al-Rub, R. K. and G. Z. Voyiadjis (2009). "Gradient-enhanced coupled plasticity-anisotropic damage model for concrete fracture: computational aspects and applications." International Journal of Damage Mechanics **18**(2): 115-154.
3. Al-Himairee, R. (2011). Characterization and Modeling of Damage in Steel at Different Strain Rates.
4. Al-Rub, A. and R. Kamel (2004). "Material length scales in gradient-dependent plasticity/damage and size effects: theory and computation."
5. Alfano, G. and M. Musto (2017). "Thermodynamic derivation and damage evolution for a fractional cohesive zone model." Journal of Engineering Mechanics **143**(7): D4017001.
6. Ali, S. M., G. Unnikrishnan and M. Joseph (2013). "Essential work of fracture of low-filled poly (methyl methacrylate)/starch composites." Journal of Applied Polymer Science **128**(3): 1409-1416.
7. Alinaghian, Y., M. Asadi and A. Weck (2014). "Effect of pre-strain and work hardening rate on void growth and coalescence in AA5052." International Journal of Plasticity **53**: 193-205.
8. Arefi, A., F. P. van der Meer, M. R. Forouzan and M. Silani (2018). "Formulation of a Consistent Pressure-Dependent Damage Model with Fracture Energy as Input." Composite Structures.
9. Arora, H., E. Tarleton, J. Li-Mayer, M. Charalambides and D. Lewis (2015). "Modelling the damage and deformation process in a plastic bonded explosive microstructure under tension using the finite element method." Computational Materials Science **110**: 91-101.
10. Ayoub, G., F. Zaïri, M. Naït-Abdelaziz, J.-M. Gloaguen and G. Kridli (2014). "A visco-hyperelastic damage model for cyclic stress-softening, hysteresis and permanent set in rubber using the network alteration theory." International Journal of Plasticity **54**: 19-33.
11. Badreddine, H., K. Saanouni and A. Dogui (2010). "On non-associative anisotropic finite plasticity fully coupled with isotropic ductile damage for metal forming." International Journal of Plasticity **26**(11): 1541-1575.
12. Bai, Y. and T. Wierzbicki (2010). "Application of extended Mohr–Coulomb criterion to ductile fracture." International Journal of Fracture **161**(1): 1.
13. Bárány, T., T. Czigány and J. Karger-Kocsis (2010). "Application of the essential work of fracture (EWF) concept for polymers, related blends and composites: A review." Progress in Polymer Science **35**(10): 1257-1287.
14. Barthelat, F. and R. Rabiei (2011). "Toughness amplification in natural composites." Journal of the Mechanics and Physics of Solids **59**(4): 829-840.
15. Basaran, C. and C.-Y. Yan (1998). "A thermodynamic framework for damage mechanics of solder joints." Journal of Electronic Packaging **120**(4): 379-384.

16. Belnoue, J. P., B. Garnham, M. Bache and A. M. Korsunsky (2010). "The use of coupled nonlocal damage-plasticity to predict crack growth in ductile metal plates." Engineering Fracture Mechanics **77**(11): 1721-1729.
17. Berezvai, S. and A. Kossa (2017). "Characterization of a thermoplastic foam material with the two-layer viscoplastic model." Materials Today: Proceedings **4**(5): 5749-5754.
18. Bergstrom, J. S. (2015). Mechanics of solid polymers: theory and computational modeling, William Andrew.
19. Bhattacharjee, T., M. Barlingay, H. Tasneem, E. Roan and K. Vemaganti (2013). "Cohesive zone modeling of mode I tearing in thin soft materials." Journal of the mechanical behavior of biomedical materials **28**: 37-46.
20. Cai, H., Y. Zhang, X. Li, J. Meng, F. Xue, C. Chu, L. Tao and J. Bai "Self-reinforced biodegradable Mg-2Zn alloy wires / polylactic acid composite for orthopedic implants." Composites Science and Technology.
21. Charalambides, M., S. Goh, L. Wanigasooriya, J. Williams and W. Xiao (2005). "Effect of friction on uniaxial compression of bread dough." Journal of Materials Science **40**(13): 3375-3381.
22. Cheng, J. and S. Ghosh (2017). "Crystal plasticity finite element modeling of discrete twin evolution in polycrystalline magnesium." Journal of the Mechanics and Physics of Solids **99**: 512-538.
23. Chivrac, F., O. Gueguen, E. Pollet, S. Ahzi, A. Makradi and L. Averous (2008). "Micromechanical modeling and characterization of the effective properties in starch-based nano-biocomposites." Acta Biomaterialia **4**(6): 1707-1714.
24. Cicekli, U., G. Z. Voyiadjis and R. K. A. Al-Rub (2007). "A plasticity and anisotropic damage model for plain concrete." International Journal of plasticity **23**(10-11): 1874-1900.
25. Danas, K. and P. P. Castañeda (2012). "Influence of the Lode parameter and the stress triaxiality on the failure of elasto-plastic porous materials." International Journal of Solids and Structures **49**(11): 1325-1342.
26. De Borst, R. and H. B. Mühlhaus (1992). "Gradient-dependent plasticity: formulation and algorithmic aspects." International Journal for Numerical Methods in Engineering **35**(3): 521-539.
27. Destrade, M., J. G. Murphy and B. Rashid (2013). "Differences in tension and compression in the nonlinearly elastic bending of beams." arXiv preprint arXiv:1303.1901.
28. Digimat, A. (2011). Software for the Linear and Nonlinear Multi-Scale Modeling of Heterogeneous Materials; e-Xstream Engineering: Louvain-la-Neuve, Belgium.
29. Dunand, M. and D. Mohr (2014). "Effect of Lode parameter on plastic flow localization after proportional loading at low stress triaxialities." Journal of the Mechanics and Physics of Solids **66**: 133-153.
30. Fernandes, E. M., R. A. Pires, J. F. Mano and R. L. Reis (2013). "Bionanocomposites from lignocellulosic resources: Properties, applications and future trends for their use in the biomedical field." Progress in Polymer Science **38**(10-11): 1415-1441.
31. Ferrara, L. and M. d. Prisco (2001). "Mode I fracture behavior in concrete: nonlocal damage modeling." Journal of engineering mechanics **127**(7): 678-692.
32. Gao, Y. and A. Bower (2004). "A simple technique for avoiding convergence problems in finite element simulations of crack nucleation and growth on cohesive interfaces." Modelling and Simulation in Materials Science and Engineering **12**(3): 453.
33. Goh, S., M. Charalambides and J. Williams (2004). "Determination of the constitutive constants of non-linear viscoelastic materials." Mechanics of Time-Dependent Materials **8**(3): 255-268.
34. Guessasma, S., M. Sehaki, D. Lourdin and A. Bourmaud (2008). "Viscoelasticity properties of biopolymer composite materials determined using finite element calculation and nanoindentation." Computational Materials Science **44**(2): 371-377.
35. Haddag, B., F. Abed-Meraim and T. Balan (2009). "Strain localization analysis using a large deformation anisotropic elastic–plastic model coupled with damage." International Journal of Plasticity **25**(10): 1970-1996.
36. Hagan, E. W. (2009). The viscoelastic properties of latex artist paints, Imperial College London.
37. Hagan, E. W., M. N. Charalambides, C. R. Young, T. J. Learner and S. Hackney (2011). "Influence of the inorganic phase concentration and geometry on the viscoelastic properties of latex coatings through the glass-transition." Polymer **52**(7): 1662-1673.

38. Hambli, R. (2013). "A quasi-brittle continuum damage finite element model of the human proximal femur based on element deletion." Medical & biological engineering & computing **51**(1-2): 219-231.
39. Harrison, S. M., P. W. Cleary, G. Eyres, M. D. Sinnott and L. Lundin (2014). "Challenges in computational modelling of food breakdown and flavour release." Food & function **5**(11): 2792-2805.
40. Hbib, M., S. Guessasma, D. Bassir and N. Benseddiq (2011). "Interfacial damage in biopolymer composites reinforced using hemp fibres: finite element simulation and experimental investigation." Composites Science and Technology **71**(11): 1419-1426.
41. He, M. and S. Li (2012). "An embedded atom hyperelastic constitutive model and multiscale cohesive finite element method." Computational Mechanics **49**(3): 337-355.
42. Hedjazi, L., S. Guessasma, G. Della Valle and N. Benseddiq (2011). "Finite element modelling of crack propagation in carbohydrate extruded starch with open void structure." Carbohydrate polymers **83**(4): 1696-1706.
43. Hillerborg, A., M. Modéer and P.-E. Petersson (1976). "Analysis of crack formation and crack growth in concrete by means of fracture mechanics and finite elements." Cement and concrete research **6**(6): 773-781.
44. Holzapfel, G. A. (2001). "Biomechanics of soft tissue." The handbook of materials behavior models **3**: 1049-1063.
45. Hurtado, J., I. Lapczyk and S. Govindarajan (2013). "Parallel rheological framework to model non-linear viscoelasticity, permanent set, and Mullins effect in elastomers." Constitutive Models for Rubber VIII **95**.
46. Ji, B. and H. Gao (2004). "Mechanical properties of nanostructure of biological materials." Journal of the Mechanics and Physics of Solids **52**(9): 1963-1990.
47. Jin, Z. (2014). Computational modelling of biomechanics and biotribology in the musculoskeletal system: biomaterials and tissues, Elsevier.
48. Ladani, L. J. and J. Razmi (2009). "An anisotropic mechanical fatigue damage evolution model for Pb-free solder materials." Mechanics of Materials **41**(7): 878-885.
49. Lapczyk, I. and J. A. Hurtado (2007). "Progressive damage modeling in fiber-reinforced materials." Composites Part A: Applied Science and Manufacturing **38**(11): 2333-2341.
50. Launey, M. E. and R. O. Ritchie (2009). "On the fracture toughness of advanced materials." Advanced Materials **21**(20): 2103-2110.
51. Lavagna, L., D. Massella, M. F. Pantano, F. Bosia, N. M. Pugno and M. Pavese (2018). "Grafting carbon nanotubes onto carbon fibres doubles their effective strength and the toughness of the composite." Composites Science and Technology.
52. Lawrimore II, W., D. K. Francis, J.-L. Bouvard, Y. Hammi and M. F. Horstemeyer (2016). "A mesomechanics parametric finite element study of damage growth and coalescence in polymers using an Elastoviscoelastic-Viscoplastic internal state variable model." Mechanics of Materials **96**: 83-95.
53. Le, D. T., J.-J. Marigo, C. Maurini and S. Vidoli (2018). "Strain-gradient vs damage-gradient regularizations of softening damage models." Computer Methods in Applied Mechanics and Engineering **340**: 424-450.
54. Lee, J.-Y., D. Steglich and M.-G. Lee (2017). "Fracture prediction based on a two-surface plasticity law for the anisotropic magnesium alloys AZ31 and ZE10." International Journal of Plasticity.
55. Luo, M. and T. Wierzbicki (2010). "Numerical failure analysis of a stretch-bending test on dual-phase steel sheets using a phenomenological fracture model." International Journal of Solids and Structures **47**(22-23): 3084-3102.
56. Lv, Z., C. Huang, H. Zhu, J. Wang, P. Yao and Z. Liu (2015). "FEM analysis on the abrasive erosion process in ultrasonic-assisted abrasive waterjet machining." The International Journal of Advanced Manufacturing Technology **78**(9-12): 1641-1649.
57. Madsen, B., R. Joffe, H. Peltola and K. Nättinen (2011). "Short cellulosic fiber/starch acetate composites—micromechanical modeling of Young's modulus." Journal of composite materials **45**(20): 2119-2131.
58. Majeed, K., M. Jawaid, A. Hassan, A. A. Bakar, H. A. Khalil, A. Salema and I. Inuwa (2013). "Potential materials for food packaging from nanoclay/natural fibres filled hybrid composites." Materials & Design **46**: 391-410.
59. Matzenmiller, A., J. Lubliner and R. Taylor (1995). "A constitutive model for anisotropic damage in fiber-composites." Mechanics of materials **20**(2): 125-152.

60. Meng, H. and G. Li (2013). "A review of stimuli-responsive shape memory polymer composites." Polymer **54**(9): 2199-2221.
61. Mohammed, I., M. Charalambides, J. Williams and J. Rasburn (2014). "Modelling the microstructural evolution and fracture of a brittle confectionery wafer in compression." Innovative Food Science & Emerging Technologies **24**: 48-60.
62. Mohammed, M. A. P., E. Tarleton, M. N. Charalambides and J. Williams (2013). "Mechanical characterization and micromechanical modeling of bread dough." Journal of Rheology **57**(1): 249-272.
63. Mohammed P. Afandi, M., L. Wanigasooriya, S. Chakrabarti-Bell and M. Charalambides (2017). "Extrusion of unleavened bread dough: Experiments and simulations." Journal of Rheology **61**(1): 49-65.
64. Mohammed P. Afandi, T., E, M. N. Charalambides and J. Williams (2013). "Mechanical characterization and micromechanical modeling of bread dough." Journal of Rheology (1978-present) **57**(1): 249-272.
65. Moscicki, L., M. Mitrus, A. Wojtowicz, T. Oniszczuk and A. Rejak (2013). Extrusion-Cooking of Starch.
66. Ogden, R. and D. Roxburgh (1999). A pseudo–elastic model for the Mullins effect in filled rubber. Proceedings of the Royal Society of London A: Mathematical, Physical and Engineering Sciences, The Royal Society.
67. Oldfield, M., D. Dini, G. Giordano and F. Rodriguez y Baena (2013). "Detailed finite element modelling of deep needle insertions into a soft tissue phantom using a cohesive approach." Computer methods in biomechanics and biomedical engineering **16**(5): 530-543.
68. Oldfield, M., D. Dini and F. R. y Baena (2010). Detailed finite element simulations of probe insertion into solid elastic material using a cohesive zone approach. Engineering in Medicine and Biology Society (EMBC), 2010 Annual International Conference of the IEEE, IEEE.
69. Pack, K., M. Luo and T. Wierzbicki (2014). "Sandia Fracture Challenge: blind prediction and full calibration to enhance fracture predictability." International Journal of Fracture **186**(1-2): 155-175.
70. Paulino, G. H., W. Celes, R. Espinha and Z. J. Zhang (2008). "A general topology-based framework for adaptive insertion of cohesive elements in finite element meshes." Engineering with Computers **24**(1): 59-78.
71. Plucknett, K. and V. Normand (2000). "Plane stress essential work of fracture of 'pseudo-ductile'gelatin/maltodextrin biopolymer gel composites." Polymer **41**(18): 6833-6841.
72. Ponnusami, S. A., S. Turteltaub and S. van der Zwaag (2015). "Cohesive-zone modelling of crack nucleation and propagation in particulate composites." Engineering Fracture Mechanics **149**: 170-190.
73. Pyo, S. and H. Lee (2010). "An elastoplastic damage model for metal matrix composites considering progressive imperfect interface under transverse loading." International journal of plasticity **26**(1): 25-41.
74. Rousselier, G. and M. Luo (2014). "A fully coupled void damage and Mohr–Coulomb based ductile fracture model in the framework of a reduced texture methodology." International Journal of Plasticity **55**: 1-24.
75. Safaei, M., M.-G. Lee and W. De Waele (2015). "Evaluation of stress integration algorithms for elastic–plastic constitutive models based on associated and non-associated flow rules." Computer Methods in Applied Mechanics and Engineering **295**: 414-445.
76. Safaei, M., J. W. Yoon and W. De Waele (2014). "Study on the definition of equivalent plastic strain under non-associated flow rule for finite element formulation." International Journal of Plasticity **58**: 219-238.
77. Sarrado, C., F. Leone, A. Turon and C. Dávila (2014). A numerical study on adhesive thickness effect on bonded joints using a modified finitethickness cohesive element. 16th European Conference on Composite Materials (ECCM16).
78. Shor, O. and R. Vaziri (2015). "Adaptive insertion of cohesive elements for simulation of delamination in laminated composite materials." Engineering Fracture Mechanics **146**: 121-138.
79. Shutov, A., C. Silbermann and J. Ihlemann (2015). "Ductile damage model for metal forming simulations including refined description of void nucleation." International Journal of Plasticity **71**: 195-217.
80. Simulia, A. V. (2013). "6.13 Documentation." Dassault systemes.
81. Simulia, D. (2013). "ABAQUS 6.13 User's Manual." Dassault Systems, Providence, RI.

82. Skamniotis, C., M. Elliott and M. Charalambides (2017). "On modeling the large strain fracture behaviour of soft viscous foods." Physics of Fluids **29**(12): 121610.
83. Skamniotis, C., M. Kamaludin, M. Elliott and M. Charalambides (2017). "A novel essential work of fracture experimental methodology for highly dissipative materials." Polymer.
84. Skamniotis, C., Y. Patel, M. Charalambides and M. Elliott (2016). "Fracture investigation in starch-based foods." Interface focus **6**(3): 20160005.
85. Skamniotis, C., Y. Patel, M. Elliott and M. Charalambides (2018). "Toughening and stiffening of starch food extrudates through the addition of cellulose fibres and minerals." Food Hydrocolloids.
86. Smojver, I. and D. Ivančević (2011). "Bird strike damage analysis in aircraft structures using Abaqus/Explicit and coupled Eulerian Lagrangian approach." Composites Science and Technology **71**(4): 489-498.
87. Su, P., Y. Yang and L. Huang (2016). "Biomechanical simulation of needle insertion into cornea based on distortion energy failure criterion." Acta of bioengineering and biomechanics **18**(1).
88. Taguet, A., M. N. Bureau, M. A. Huneault and B. D. Favis (2014). "Toughening mechanisms in interfacially modified HDPE/thermoplastic starch blends." Carbohydrate polymers **114**: 222-229.
89. Tanaka, Y. (2007). "A local damage model for anomalous high toughness of double-network gels." EPL (Europhysics Letters) **78**(5): 56005.
90. van Dongen, B., A. van Oostrum and D. Zarouchas (2018). "A blended continuum damage and fracture mechanics method for progressive damage analysis of composite structures using XFEM." Composite Structures **184**: 512-522.
91. Verhoosel, C. V., M. A. Scott, T. J. Hughes and R. De Borst (2011). "An isogeometric analysis approach to gradient damage models." International Journal for Numerical Methods in Engineering **86**(1): 115-134.
92. Vignjevic, R., N. Djordjevic, S. Gemkow, T. De Vuyst and J. Campbell (2014). "SPH as a nonlocal regularisation method: Solution for instabilities due to strain-softening." Computer Methods in Applied Mechanics and Engineering **277**: 281-304.
93. Vignjevic, R., N. Djordjevic and V. Panov (2012). "Modelling of dynamic behaviour of orthotropic metals including damage and failure." International Journal of Plasticity **38**: 47-85.
94. Voyiadjis, G. Z. (2012). Advances in damage mechanics: metals and metal matrix composites, Elsevier.
95. Voyiadjis, G. Z. and R. J. Dorgan (2004). "Bridging of length scales through gradient theory and diffusion equations of dislocations." Computer methods in applied mechanics and engineering **193**(17-20): 1671-1692.
96. Voyiadjis, G. Z. and P. I. Kattan (1992). "A plasticity-damage theory for large deformation of solids? I. Theoretical formulation." International Journal of Engineering Science **30**(9): 1089-1108.
97. Voyiadjis, G. Z., A. Shojaei and G. Li (2011). "A thermodynamic consistent damage and healing model for self healing materials." International Journal of Plasticity **27**(7): 1025-1044.
98. Wang, S. and S. A. Chester (2017). "Experimental characterization and continuum modeling of inelasticity in filled rubber-like materials." International Journal of Solids and Structures.
99. Wang, X., M. Zhang and A. P. Jivkov (2016). "Computational technology for analysis of 3D meso-structure effects on damage and failure of concrete." International Journal of Solids and Structures **80**: 310-333.
100. Wheatley, B. B., D. A. Morrow, G. M. Odegard, K. R. Kaufman and T. L. H. Donahue (2016). "Skeletal muscle tensile strain dependence: Hyperviscoelastic nonlinearity." Journal of the mechanical behavior of biomedical materials **53**: 445-454.
101. Xue, Z., M. Pontin, F. Zok and J. W. Hutchinson (2010). "Calibration procedures for a computational model of ductile fracture." Engineering Fracture Mechanics **77**(3): 492-509.
102. Yao, W. and C. Basaran (2013). "Computational damage mechanics of electromigration and thermomigration." Journal of Applied Physics **114**(10): 103708.
103. Zaïri, F., M. Naït-Abdelaziz, J.-M. Gloaguen and J.-M. Lefebvre (2008). "Modelling of the elasto-viscoplastic damage behaviour of glassy polymers." International Journal of Plasticity **24**(6): 945-965.
104. Zakaria, N., N. Muhammad and M. Abdullah (2017). Potential of Starch Nanocomposites for Biomedical Applications. IOP Conference Series: Materials Science and Engineering, IOP Publishing.
105. Zhang, T., S. Lin, H. Yuk and X. Zhao (2015). "Predicting fracture energies and crack-tip fields of soft tough materials." Extreme Mechanics Letters **4**: 1-8.

106. Zhao, F., D. Yao, R. Guo, L. Deng, A. Dong and J. Zhang (2015). "Composites of polymer hydrogels and nanoparticulate systems for biomedical and pharmaceutical applications." Nanomaterials **5**(4): 2054-2130.